Collagen remodeling leads to inflammation-free expansion of periprostatic adipose tissue and promotes prostate cancer progression

David Estève[1], Aurélie Toulet[1], Mathieu Roumiguié[1,2], Dawei Bu[3], Sarah Pericart[4], Chloé Belles[5], Cécile Manceau[1,2], Cynthia Houël[1], Manuelle Ducoux-Petit[1,6], Nathalie Van Acker[4], Stéphanie Dauvillier[1], Yiyue Jia[1], Camille Franchet[4], Nicolas Doumerc[2], Mathieu Thoulouzan[2], Sophie Le Gonidec[7], Philippe Valet[7], Bernard Malavaud[2], Odile Burlet-Schiltz[1,6], Anne Bouloumié[5], Philipp E. Scherer[3], Delphine Milhas[1], Catherine Muller[1]

[1]Institut de Pharmacologie et de Biologie Structurale (IPBS), Université de Toulouse, CNRS, Université Toulouse III - Paul Sabatier (UPS), Toulouse, France. Équipe Labélisée Ligue Nationale contre le Cancer.
[2]Department of Urology and Renal Transplantation, Toulouse University Hospital ; Institut Universitaire du Cancer de Toulouse, Oncopole, Toulouse, France.
[3]Touchstone Diabetes Center, Department of Internal Medicine and Department of Cell Biology, University of Texas Southwestern Medical Center, Dallas, TX, USA.
[4]Department of Pathology, Institut Universitaire du Cancer de Toulouse, Oncopole, Toulouse, France.
[5]Institut des Maladies Métaboliques et Cardiovasculaires, Université de Toulouse, INSERM, UPS, Toulouse, France
[6]Infrastructure Nationale de Protéomique, ProFI, FR 2048, Toulouse, France
[7]Institut RESTORE, Université de Toulouse, CNRS U-5070, EFS, ENVT, INSERM U1301, UPS, Toulouse, France.

Address correspondance to : Catherine Muller, IPBS CNRS UMR 5089, 205 route de Narbonne, 31077 Toulouse, France. Phone: 33.561.17.59.32; E-mail: muller@ipbs.fr or to: Delphine Milhas, IPBS CNRS UMR 5089, 205 route de Narbonne, 31077 Toulouse. Phone: 33-561-17-58-66 ; E-mail: milhas@ipbs.fr

Summary
The abundance of periprostatic adipose tissue favors prostate cancer aggressiveness. The increase in extracellular matrix remodeling that occurs in expanded periprostatic fat allows adipocyte hypertrophy without tissue inflammation and generates a matrikine, endotrophin, which favors tumor progression.

Abstract

Periprostatic adipose tissue (PPAT) abundance correlates with prostate cancer progression, but the mechanism remains unexplained. Here, we used a statistical approach to define abundant PPAT by normalizing PPAT volume to prostate volume in a cohort of 351 patients with a linear regression model. Applying this definition, we find tumors specifically from patients with abundant PPAT exhibit several hallmarks of aggressiveness, suggesting that PPAT abundance might be used to improve risk stratification. We show that abundant PPAT expands by adipocyte hypertrophy but this does not result in inflammation. Extensive extracellular matrix remodeling, notably of the collagen network, and decreased expression of mechano-sensing proteins in adipocytes explains this inflammation-free expansion by decreasing the mechanical constraints on the adipocytes. Moreover, collagen VI degradation in abundant PPAT is associated with production of endotrophin, a matrikine that promotes cancer progression. We find high levels of endotrophin specifically in the urine of patients with abundant PPAT, indicating the clinical relevance of our findings.

Introduction

Prostate cancer (PCa) is the second most common form of solid tumor in men worldwide and the fifth leading cause of death from cancer (Pernar et al., 2018). It is a highly heterogeneous disease, ranging from slow-growing indolent tumors to fatal metastatic carcinomas (Pernar et al., 2018). Risk stratification is, therefore, the cornerstone for selecting the most appropriate treatment for these men. Progression from indolent to aggressive PCa depends on endocrine signaling (mainly through the androgen receptor) and genetic alterations leading to cancer cell-autonomous progression (Pernar et al., 2018) ; however, paracrine signaling from the tumor microenvironment also plays a role (Shiao et al., 2016). The adipose tissue (AT) surrounding the prostate, called periprostatic adipose tissue (PPAT), has emerged recently as an important factor in the progression of the disease (Estève et al., 2020). Like other white adipose tissue (WAT), PPAT comprises mainly adipocytes and other cell types in the stromal vascular fraction, including adipose progenitor cells, fibroblasts, endothelial and immune cells, all of which are embedded in the extracellular matrix (ECM) (Zwick et al., 2019). Also, as a WAT, PPAT is an active metabolic and secretory organ (Zwick et al., 2019; Nassar et al., 2018).

Both clinical and fundamental biological studies have shown that PPAT contributes to the progression of PCa. Extension of the prostate tumor into PPAT is an important indicator of a poor prognosis (Kapoor et al., 2013). PPAT promotes prostate tumor aggressiveness and local dissemination by secreting soluble factors such as chemokines (Laurent et al., 2016), pro-inflammatory cytokines (Gucalp et al., 2017) and lipid mediators (Laurent et al., 2019) (for review, (Estève et al., 2020). Also, in obese patients, the secretory and metabolic dysfunctions of PPAT amplify the involved mechanisms (Estève et al., 2020; Gucalp et al., 2017; Laurent et al., 2016, 2019). Several meta-analyses have established an association between obesity and increased risk of PCa recurrence, progression to advanced cancer, and PCa-related mortality (Cao and Ma, 2011; Harrison et al., 2020). The increased risk of advanced disease and PCa-specific mortality ranges from 6-12 % with every 5 kg/m^2 increase in body mass index (BMI) (Cao and Ma, 2011; Harrison et al., 2020). Although changes in PPAT function occur in obesity (Estève et al., 2020), many studies have shown that, unlike all other WAT, the volume of PPAT, as measured by multiparametric magnetic resonance imaging (mpMRI), does not correlate with BMI (Woo et al., 2015; Roumiguié et al., 2022; Zhang et al., 2014). This failure of PPAT to expand in obese individuals may be explained by the chronic hypoxic state of PPAT, which induces fibrosis (Roumiguié et al., 2022).

Although the volume of PPAT in an individual does not correlate with his BMI, it does vary considerably between individuals (Zhang et al., 2014; Woo et al., 2015; Roumiguié et al., 2022). Recent clinical studies have demonstrated that patients with large amounts of PPAT have more aggressive PCa than the patients with low amounts (Nassar et al., 2018), suggesting that the abundance of PPAT might be used to stratify patients' risk. PPAT abundance correlates with prostate tumors with high Gleason

scores and local dissemination (Nassar et al., 2018; Zhang et al., 2014; Woo et al., 2015; Van Roermund et al., 2011; Zhai et al., 2021), which are indicators of high risk progression. Measurement of PPAT abundance may be used in the early management of PCa patients since it predicts PCa aggressiveness in patients undergoing radical prostatectomy (RP) for localized disease (Dahran et al., 2019; Zhai et al., 2018) and predicts progression-free survival in men with indolent PCa who are under active surveillance (Gregg et al., 2021). Moreover, in advanced PCa, the abundance of PPAT may be a predictor of the cancer's resistance to castration (Salji et al., 2018; Sasaki et al., 2020; Huang et al., 2019). Considered together, these studies suggest that the expansion of PPAT might be far more important than obesity in determining the progression of PCa and its outcome for the patient.

The recognition of an important relationship between PPAT abundance and PCa raises several important issues (Dahran et al., 2017). First, no consensus has emerged from the literature about the most appropriate way to quantify PPAT abundance, making it difficult to compare directly the findings of different studies and potentially limiting translation of this concept from clinical studies into practice. Several methods have been reported, including measuring the area of PPAT in a single slice image obtained by computed tomography (Van Roermund et al., 2011) or mpMRI (Zhang et al., 2014), and simply measuring the thickness of PPAT by mpMRI (Woo et al., 2015). More recently, calculating the whole PPAT volume from successive mpMRI slices by using appropriate software has been proposed as a more accurate method (Dahran et al., 2019; Zhai et al., 2018; Gregg et al., 2021; Salji et al., 2018) . As PPAT volume is reported to correlate with prostate volume (Dahran et al., 2017; Tan et al., 2016), several studies have used the ratio of PPAT volume to prostate volume in an individual – the normalized periprostatic fat volume (NPFV) (Dahran et al., 2017; Tan et al., 2016) – to compare PPAT abundance between individuals. Second, the biological mechanisms that result in expansion of PPAT and the role of abundant PPAT in PCa progression are still unknown.

In this study, we developed a more refined definition of abundant PPAT that might be applicable both in basic research and for risk stratification in the clinic. Using this definition, we characterize the differences between abundant PPAT and less abundant PPAT in PCa patients to shed light on the role of abundant PPAT in the aggressiveness of PCa. We find that tissue expansion in abundant PPAT is due to adipocyte cell enlargement, or hypertrophy, which, unlike expansion of other WAT, does not drive inflammation. This inflammation-free expansion of PPAT is explained by extensive remodeling of the ECM, in particular degradation of collagen, which reduces the mechanical constraints on the adipocytes, and generates a matrikine, endotrophin, which promotes tumor progression.

Results

A new statistical approach to defining abundant PPAT relative to prostate volume

To define PPAT abundance more precisely, we wanted to develop a measure that expresses the volume of PPAT with respect to the volume of the prostate normalized to a population rather than to an individual. To do so, we examined a cohort of 351 patients awaiting prostatectomy for PCa by using pre-operative mpMRI, from which we measured prostate and PPAT volume within well-defined anatomical limits (Table S1 and Fig. 1A). We found a strong correlation between the volume of the prostate determined by mpMRI before prostatectomy and its weight after prostatectomy (Fig. 1B), thus validating the accuracy of the measurement method. A group of 20 patients that underwent mpMRI for non-oncological pathologies were also included in the study. In the cohort of PCa patients, PPAT volume was independent of BMI (Fig. 1C), as we reported previously for a smaller cohort (Roumiguié et al., 2022); this was true also for the patients without PCa (Fig. 1C). In both groups of patients, subcutaneous AT area (Fig. S1A) and perirectal AT area (Fig. S1B) both correlated with BMI. PPAT volume correlated with prostate volume in both groups of patients (Fig. 1D), thus this relationship is independent of the presence of PCa. Based on this strong correlation between PPAT volume and prostate volume, we modeled the expected PPAT volume according to the prostate volume by using a linear regression model and calculated PPAT abundance with the residual values from this model. The residual values are a measure of the difference between the volume of PPAT quantified by mpMRI and the amount of PPAT predicted by the model (Fig. 1E). The cohort was divided into quartiles according to residuals values allowing to identify patients with the least PPAT in the 1st quartile (low PPAT) and patients with the most PPAT in the 4th quartile (high PPAT) (Fig. 1 E-F). Patients in the 2nd and 3rd quartile were classified as having a mid PPAT abundance (Fig. 1 E-F). No differences were observed between patients in the four quartiles when we analyzed prostate volume (Figure 1G), BMI (Figure 1H) or age (Figure 1I).

In our PCa cohort, NPFV only partially reflected PPAT abundance as calculated by our model (Fig. S2A). When we ranked our patients according to ascending NPFV, some patients with the highest NPFVs fell into our mid PPAT group, whereas others with relatively low NPFVs fell into our high PPAT group (Fig. S2A). Overall, nearly 30% of patients fell into different groups when analyzed by the two methods (Fig. S2A). To investigate further the differences between the two methods, we assigned the individuals in our cohort to quartiles based on ascending NPFV: 1st quartile (low NPFV), 2nd and 3rd quartile (mid NPFV) and 4th quartile (high NPFV). When we plotted the PPAT volumes of the individuals in each quartile, we saw no difference between the mean PPAT volumes of the quartiles (Fig. S2B), whereas prostate volume decreased as NPFV increased (Fig. S2C). Thus, large NPFVs are due primarily to small prostate volumes rather than large PPAT volumes, unlike our model.

Abundant PPAT is associated with aggressive tumors

To evaluate the relationship between PPAT abundance, as defined above, and PCa aggressiveness, we compared abundance to the clinical and pathological parameters of the patients in our cohort (Table S2). This cohort included only patients who underwent prostatectomy, because we wanted to perform histological and biochemical analyses on the excised tissues. The cohort was rather homogenous in the aggressiveness of their cancers, according to current prostatectomy indications (Costello, 2020). The Gleason score, one of the main criteria to evaluate the prognosis of a PCa, is based on hematoxylin and eosin (HE) staining of tumor sections and evaluate the differentiation and architecture of the tumor; it is used to determine the ISUP (International Society of Urological Pathology) grade (1-5). Most patients in our PCa cohort were graded 2 or 3 on the ISUP scale (Table S2). Nevertheless, the proportion of patients with an ISUP grade ≥ 3 increased with PPAT abundance and was significantly different between the low PPAT and high PPAT groups (Fig. 2A and Table S3). In addition to the ISUP score, the percentage of undifferentiated cancer cells in the tumors of patients in the high PPAT group was significantly greater than it was in the patients in the low PPAT group (Fig. 2B and Table S3). Moreover, there was a significant association between the abundance of PPAT and the concentration of prostate-specific antigen in the blood of patients with PCa prior to surgery (Table S3). Taken together, these data indicate that abundant PPAT, as defined by our method, correlates with more aggressive tumors, suggesting that it might play a role in PCa progression.

To evaluate the potential value of our PPAT abundance measure for predicting the ISUP score, we compared the ISUP grade of tumor tissue obtained after prostatectomy with that determined on pre-operative biopsied tissue in a subset of patients with ISUP grades < 3 (i.e. less aggressive prostate cancer), then determined the percentage of patients in low, mid and high PPAT groups whose ISUP scores were upgraded after surgery (Fig. 2C). The proportion of patients whose ISUP scores were upgraded increased from 15% in the low PPAT group to 39% in the high PPAT group, suggesting that PPAT abundance might be a useful criterion to improve risk stratification. Multivariate analysis using a logistic regression model found that PPAT abundance was an independent risk factor for PCa with an ISUP score ≥ 3 (Fig. 2D), whereas NPFV was not (Fig. S2D). In addition, NPFV was not associated to PCa aggressiveness (Table S4).

Accumulating evidence indicates that mechanisms underlying the progression of PCa are not confined to epithelial cells but also involve the tumor microenvironment (Shiao et al., 2016). We found above that the abundance of PPAT correlated with the occurrence of tumors with a high Gleason grade, but this grade considers only the epithelial component of the tumor. To investigate whether the microenvironment differs in tumors associated with abundant PPAT when compared to those with less

abundant PPAT, we used histochemistry and immunohistochemistry of sections of paraffin-embedded tumors to analyze ECM deposition (Masson's trichrome staining; Fig. 2E), angiogenesis (anti-CD31 staining, Figure 2F) and macrophage infiltration (anti-CD68 staining, Fig. 2G); all three are hallmarks of cancer aggressiveness. Quantification of Masson's trichrome staining, which stains fibrillar collagens blue, indicated enhanced collagen deposition in tumors from patients in the high PPAT group when compared with that of patients in the low PPAT group (Fig. 2D). Likewise, immunostaining with anti-CD31 and anti-CD68 antibodies showed greater blood vessel density and macrophage infiltration, respectively, in tumors from patients in the high PPAT group than in those in the low PPAT group (Fig. 2E-F). Overall, the tumors from patients in the high PPAT group exhibited several hallmarks of aggressiveness including modifications of glandular architecture and dedifferentiation of the epithelial compartment as reflected in the ISUP score, fibrosis, dense vascularization and high levels of macrophage infiltration into the tumors.

PPAT expands by adipocyte hypertrophy with no associated inflammation

AT expands in response to surplus energy by two main mechanisms: adipocyte enlargement, or hypertrophy, and adipocyte hyperplasia, in which new adipocytes are recruited by adipogenesis from progenitors (Pellegrinelli et al., 2016). The balance between hypertrophy and hyperplasia depends on the adipose depot concerned (Pellegrinelli et al., 2016). To distinguish between these two mechanisms of expansion in PPAT, we stained paraffin-embedded PPAT sections with HE and measured the diameters of the adipocytes by a semi-automated method, Adiposoft© (Fig. 3A). The adipocyte size distribution curve was shifted towards larger cells in PPAT from patients in the high PPAT group when compared with those in the low PPAT group, and the mean adipocyte diameter was larger (Fig. 3B), indicating adipocyte hypertrophy. To analyze whether adipocyte hyperplasia was also occurring, we digested PPAT with collagenase to separate adipocytes from the stromal vascular fraction, which contains the adipose progenitors. The cells in the stromal vascular fraction were immunostained with antibodies against the markers CD45, CD34 and CD31 and analyzed by flow cytometry. The percentage of cells in this fraction that were progenitor cells (defined as CD45-/CD34+/CD31- cells) was similar in PPAT from patients in the various groups (Fig. 3C). Furthermore, when additional markers (MSCA1 and CD271) were used to characterize the sub-populations of adipose progenitors (Estève et al., 2019), the proportions of the various progenitor subsets (the adipogenic, MSCA1+; myofibrogenic MSCA1-/CD271+, and immature MSCA1/CD271- subsets), were similar in all groups (Fig. S3A), indicating no increased adipogenesis from progenitors in abundant PPAT. We conclude that adipocyte hypertrophy rather than hyperplasia is the mechanism of PPAT expansion in patients with abundant PPAT.

Adipocyte hypertrophy during AT expansion is usually associated with changes in secretion related to AT dysfunction (Ouchi et al., 2011). Key among these changes is increased secretion of leptin and, in parallel, decreased secretion of adiponectin (Frühbeck et al., 2019). The decrease in the ratio of adiponectin/leptin secretion has been proposed as a marker of dysfunctional AT in metabolic disorders and inflammation (Frühbeck et al., 2019; Zhao et al., 2021). Despite the adipocyte hypertrophy we saw in PPAT from patients in the high PPAT group, more adiponectin was secreted by this PPAT than by PPAT from patients in the low PPAT group (Fig. 3D), whereas leptin secretion by both tissues was similar (Fig. 3E). Accordingly, the adiponectin/leptin secretion ratio was greater in high than in low PPAT (Fig. 3F). Thus, the adipocyte hypertrophy observed in high PPAT is not associated with the changes in secretion that are usually observed in dysfunctional AT.

The proportion of immune system cells in AT generally increases as the tissue expands and this is associated with the onset of chronic low-grade inflammation (Ouchi et al., 2011). We measured the proportion of immune cells in PPAT from patients in the three groups by immunostaining the cells in the stromal vascular fraction with antibodies against CD45 and other specific markers of immune population subsets and analyzed them by flow cytometry. The proportion of CD45+ leukocytes in this fraction was similar in the various groups of patients (Fig. 3G), as was the proportion of total lymphocytes (defined as CD45+/low side scatter) (Fig. 3H) and of various lymphocyte subsets (Figure S3B). The proportion of macrophages (defined as CD45+/CD14+ cells), including the sub-populations that express or do not express CD206, were also similar in the various groups (Fig. 3I). These data indicate that PPAT expansion is not associated with increased immune cell infiltration.

To characterize further the inflammatory state of abundant PPAT, we quantified secretion of several proinflammatory cytokines by PPAT from patients in the various groups. No significant differences were seen between the amounts of TNF-α, IL6, or MCP-1 secreted (Fig. 3 J-L), and the tissue from patients in the high PPAT group secreted slightly less IL1β than did the others (Fig. 3M). Thus, the PPAT from patients in the high PPAT group does not secrete more proinflammatory cytokines than the PPAT from the patients in the mid and low PPAT groups. Together, these data indicate that although PPAT expands by adipocyte hypertrophy, this expansion does not cause the inflammation observed in other ATs that expand by this mechanism.

Under-representation of mechano-sensing proteins in adipocytes from abundant PPAT

According to our findings described above, adipocytes are the main cell type that changes in the PPAT from patients in the high PPAT group. To investigate further the changes in the adipocytes, we isolated adipocytes from the PPAT of patients in the high PPAT and low PPAT groups and analyzed them by proteomics. Principal component analysis of the proteomics dataset separated the patients according to

the abundance of their PPAT (Fig. 4A). Component 1, which separated the patients according to their PPAT groups, explained 52% of the variance in the proteomic dataset (Fig. 4A). Whereas the low PPAT patients grouped closely on the scatter plot, those with high PPAT spread widely (Fig. 4A). Of the 4033 proteins identified by proteomics, statistical analysis found 352 whose abundance differed in PPAT from patients in the high and low PPAT groups: 157 were over-represented and 195 were under-represented in the samples from the high PPAT group when compared to those from the low PPAT group (Fig. 4B). Hierarchical clustering by using Ward's method on differentially represented proteins grouped the samples according to their abundance status (Fig. 4C).

To characterize further the differences between adipocytes in the PPAT of patients in the high and low PPAT groups, we used gene ontology enrichment analysis of the proteomics dataset to identify cellular components and molecular functions. We found large differences in the abundance of proteins involved in cytoskeletal organization, cell-ECM interactions and, to a lesser extent, lipid metabolism (Fig. 4D). From this analysis, the main characteristics of adipocytes from abundant PPAT can be described as having, foremost, an under-representation of proteins involved in mechano-transduction and sensing stiffness (ontology terms in bold in Fig. 4D). Among them, YAP1 (Yes-associated protein 1) is the most under-represented protein in the PPAT of patients in the high PPAT group (log2 fold-change = -5.8) when compared with the low PPAT group (Fig. 4E). YAP1 is a key mechano-transducer that senses mechanical stimuli and relays them to regulate transcription and, thus, many aspects of cell behavior (Dupont et al., 2011). ZYXIN (Ma et al., 2016) and PACSIN2 (Rausch and Hansen, 2020), proteins that participate in the nuclear translocation and activation of YAP1 upon mechanical stress, were also significantly under-represented in the most abundant PPAT, as was ROCK2, a target of YAP/TEAD transcriptional complex (Dupont et al., 2011) (Fig. 4E). We confirmed by immunofluorescence microscopy that PPAT from patients in the high PPAT group contained much less YAP1 than that from patients in the low PPAT group (Fig. 4F).

The second important characteristic of adipocytes from abundant PPAT identified by pathway enrichment analysis was under-representation of several tubulin isoforms (Fig. 4G), which was accompanied by altered microtubule organization seen by immunofluorescence microscopy (Figure 4H). Proteins involved in cytoskeletal organization, such as cortactin (CTTN), an actin nucleation factor that influences the stability of actin filaments, and members of the vinexin family (SORBS-1 and SORBS-3), which are involved in contractile force generation in response to mechanical stress (Ichikawa et al., 2017) were also under-represented (Fig. 4I).

A third notable characteristic of adipocytes from the high PPAT group was the abundance of proteins involved in lipid metabolism (Fig. 4D), which may explain, at least in part, the observed adipocyte hypertrophy. Several key proteins involved in lipolysis were under-represented in PPAT from patients

in the high PPAT group, including adipocyte triglyceride lipase (encoded by *PNPLA2*), hormone-sensitive lipase (encoded by *LIPE*), perilipin1 (encoded by PLIN1) and Abhydrolase domain-containing protein 5 (encoded by ABHD5) (Fig. S4A). For PNPLA2 and LIPE, a downward trend regulation at mRNA levels according to abundance status was confirmed by RT-qPCR, whereas the level of MGLL (encoding Monoacylglycerol Lipase) was unchanged (Fig. S4B). By contrast, adiponectin (encoded by ADIPOQ) and several lipid transporters that take up fatty acids like CD36 or FABP4 (Fatty Acid Binding protein 4) were over-represented and regulation of their mRNA levels according to abundance status was confirmed by RT-qPCR and similar differences were also observed for the Long-chain fatty acid transport protein 4 (encoded by SLC27A4) (Fig. S4A and S4C).

The collagen network in abundant PPAT is relatively loose

We deduce from the data described above that abundant PPAT might be subject to fewer mechanical constraints (as indicated by the under-representation of proteins involved in mechano-sensing and cytoskeletal contractile force generation) than in less abundant PPAT, which may account for its expansion without inflammation. To investigate this hypothesis, we examined the collagen networks of PPAT from patients in the high and low PPAT groups. Collagen is the most abundant ECM protein and excessive collagen deposition provides tissue rigidity. We stained the collagen fibers with picrosirius red, imaged the staining by 3D confocal microscopy and reconstructed images of the fiber network in 3D. In the reconstructions, the signal from collagen fibers was weaker in PPAT from patients in the high PPAT group than it was in the patients in the low PPAT group (as shown by the maximum intensity projection), and the collagen network was substantially less dense and had thinner fibers (Fig. 5A). These observations were verified by using Imaris software to quantify the volume and length of the collagen fibers as well as the total number of branches seen in the 3D reconstructions (Fig. 5 B–D). To confirm our findings further, we used a different approach based on quantification of hydroxyproline, a measure of the collagen content of the tissue. Consistent with the imaging analysis of the collagen fiber network, we found significantly less hydroxyproline in PPAT from patients in the high PPAT group than in patients in the low PPAT group (Fig. 5E). Together, these analyses indicate that abundant PPAT has a looser collagen network than less abundant PPAT, supporting the hypothesis that mature adipocytes in abundant PPAT are subject to fewer mechanical constraints than those in less abundant PPAT.

Abundant PPAT exhibits increased collagen degradation likely by MMP9

Our findings indicate that abundant PPAT contains less collagen organized in a looser network than in less abundant PPAT. To determine whether this reflects less collagen synthesis or more degradation of

the proteins, we used RT-qPCR to compare the expression of the genes encoding the major fibrillar collagens (*COL1A1* and *COL3A1*) as well as the 3 different alpha chain of the most abundant non-fibrillar collagen, collagen VI (Sun et al., 2013) (*COL6A1*, *COL6A2* and *COL6A3*) in PPAT from patients in the high and low PPAT groups. We saw no differences between them (Fig. 6A) suggesting that the smaller amount of collagen and looser network in abundant PPAT is not due to less synthesis but may be due to increased degradation.

To investigate this hypothesis, we stained PPAT samples with a fluorescent peptide (F-CHP) that binds specifically to denatured collagen strands (Hwang et al., 2017) and imaged the staining by 3D confocal microscopy. The images showed a punctate staining located alongside fibrillar structures in PPAT from patients in the high PPAT group, whereas very weak signals were seen in PPAT from patients in the low PPAT group (Fig. 6B, left panel). Quantification of the signals from F-CHP after 3D reconstruction confirmed the substantial increased in collagen degradation in PPAT from the high PPAT group when compared with the low PPAT group (Fig. 6B, right panel).

Matrix metalloproteinases are the main enzymes involved in collagen degradation. To investigate the potential involvement of various matrix metalloproteinases in the degradation of collagen in high PPAT, we quantified expression of the main metalloprotease genes expressed in AT (*MMP-2*, *MMP-9*, *MMP-11*, *MMP-14* and *BMP1*) by RT-qPCR. Significantly more *MMP9* mRNA was found in PPAT from patients in the high PPAT group than in PPAT from patients in the low PPAT group (Fig. 6C). This was confirmed by analyzing the proteomics data from isolated adipocytes (Fig. 6D), and it was reflected in elevated MMP9 activity (Fig. 6E). MMP activity is tightly regulated by the balance between expression of the genes encoding MMPs and their endogenous inhibitors the TIMPs (tissue inhibitor of metalloproteinases). Therefore, we analyzed the expression of the genes encoding various TIMP isoforms as well as those encoding the lysyl oxidases LOX and LOXL1, which cross-link ECM proteins. All these genes were expressed at similar levels in the high and low PPAT groups (Fig. S5). We conclude that the smaller amount of collagen in abundant PPAT than in less abundant PPAT and its disorganization is due to enhanced degradation that likely involves MMP9.

COL6 remodeling is associated with high endotrophin production in abundant PPAT

ECM remodeling generates bioactive fragments called matrikines that are implicated in cancer (Ricard-Blum and Salza, 2014). The matrikine endotrophin, for example, is generated by proteolytic cleavage of the C-terminal part of COL6a3 and is implicated in malignant tumor growth and progression (Bu et al., 2019; Park and Scherer, 2012). In breast cancer, endotrophin produced by AT affects both the cancer cells, by inducing epithelial to mesenchymal transition, and the tumor microenvironment, by causing fibrosis and recruiting macrophages and endothelial cells (Bu et al., 2019; Park and Scherer, 2012). These

features are reminiscent of the hallmarks of tumors associated with high PPAT, including dedifferentiation (as seen in Fig. 2A-B) and modifications of the microenvironment (Fig. 2D-F). Thus, we postulated that endotrophin might be involved in PCa progression in patients with abundant PPAT. To investigate this possibility, we first compared COL6 in PPAT tissue from patients in the high PPAT group with that in the low PPAT group by immunofluorescence staining and 3D confocal microscopy. The COL6 staining was weaker in the high PPAT group than in the low PPAT group, it was punctiform and the COL6 microfibrils were clearly disorganized (Fig. 7A), confirming that COL6 is degraded in abundant PPAT. To determine whether this degradation generated endotrophin, we immunostained the tissue with an antibody specific for endotrophin (Bu et al., 2019) and imaged by immunofluorescence microscopy (Fig. 7B). Much more endotrophin was seen in PPAT from patients in the high PPAT group than in that from patients in the low PPAT group (Fig. 7B), consistent with the notion that this matrikine is involved in PCa progression in patients with abundant PPAT.

To investigate the clinical relevance of our findings, we quantified endotrophin in biological fluids from patients with PCa who had been diagnosed by mpMRI (see Table S5-6 for the description of the new cohort). After quantification of endotrophin, the patients were classified into the low, mid and high PPAT groups defined above. Endotrophin plasma levels were similar in all patients regardless of their PPAT abundance status (Fig. 7C). By contrast, the endotrophin concentration in urine collected after prostate massage, that causes exfoliation of cells from the tumor into biological fluids (Fujita and Nonomura, 2018), was greater in patients in the high PPAT group than it was in patients in the low PPAT group (Fig. 7D). We conclude that patients with PCa and abundant PPAT produce more endotrophin than patients with less abundant PPAT. Together, our findings suggest a model in which the extensive collagen remodeling that occurs in abundant PPAT generates endotrophin, which increases the aggressiveness of the adjacent PCa tumors.

Discussion

Several studies have concluded that excessive fat around the prostate plays a role in PCa progression and outcome, despite differences in the methods and criteria that were used to define PPAT abundance (Nassar et al., 2018). Here, we developed a statistical definition of abundant PPAT as an excess of PPAT volume when compared to the prostate volume predicted from a large cohort of patients. We show that abundant PPAT expands by adipocyte hypertrophy but this does not cause inflammation, since changes in the ECM relieve the mechanical constraints on the expanded tissue as shown by the decrease in proteins involved in mechanical sensing and cytoskeleton organization and forces. This ECM remodeling in abundant PPAT is associated with increased expression and activity of the matrix protease MMP9 and results in generation of a matrikine, endotrophin, which, in other cancer types,

promotes the epithelial–mesenchymal transition and shapes a microenvironment that favors cancer progression (Funcke and Scherer, 2019; Wang and Pan, 2020). The presence of large amounts of endotrophin in the urine of patients with abundant PPAT reinforces the clinical relevance of our findings. Our main findings and the mechanism we propose are summarized in Figure 8.

To develop a definition of PPAT abundance that might be generally acceptable to the field and that might be used in clinical practice, we used mpMRI – the gold standard for imaging the prostate and surrounding tissues – to measure both prostate volume and the whole volume of PPAT rather than simply the thickness of fat or the area of the tissue at a single point. We measured these volumes by applying a slice-by-slice segmentation technique used previously in one study (Dahran et al., 2017), and used Denonvillier's fascia, the anatomical barrier between the prostate and the other part of pelvic region, as the posterior limit of the PPAT, the definition of which varied in previous studies. Using this approach, we demonstrate that the volume of the PPAT correlates with that of the prostate. As prostate size is highly variable between individuals and often increases with age (Loeb et al., 2009), some previous studies used the ratio between the PPAT volume or area and the prostate size of the individual as a way of normalizing PPAT abundance (Zhai et al., 2021; Dahran et al., 2017). We show that this approach introduces a bias towards patients with smaller prostates being identified as having abundant PPAT, consistent with the findings of a previous study (Dahran et al., 2017). To overcome this bias, we developed a linear regression model that normalizes PPAT abundance by comparing the residual value of PPAT volume to the linear relationship between PPAT and prostate volume computed from the whole cohort. Using this approach, we calculated PPAT abundance for each individual in the cohort, ranked the population according to PPAT abundance and divided it into quartiles. We observed no differences in prostate size, BMI, or age and between the patients in these quartiles, thus validating our approach.

Applying our new approach to define PPAT abundance, we find that patients with the most abundant PPAT, i.e. those in the top quartile or the high PPAT group, have the most aggressive PCa (as defined by ISUP scores and percentage of undifferentiated cells) and that this measure of PPAT abundance predicts whether a patient's ISUP score was upgraded after RP. More importantly, PPAT abundance was an independent risk factor for PCa with an ISUP score ≥ 3. As described below, PCa management suffers from the lack of strong criteria to overcome prognostic heterogeneity and to tailor the treatment strategy. Since mpMRI is now widely used prior to biopsies, the measurement of PPAT volume should be evaluated as a prognostic marker for these localized PCa in order to evaluate if these high-risk patients will benefit from additional therapies. Since we wanted to perform biological characterization of PPAT, our cohort included only patients who underwent prostatectomy and excluded patients with a low ISUP score (ISUP 1), who may choose active surveillance rather than treatment, and those with

highly aggressive disease (ISUP 4 or 5), who often have advanced local or distant dissemination of their tumors. A large clinical study, including unsorted patients and automation of the method, would be necessary to establish the utility of PPAT measurement in PCa risk stratification in all these different clinical situations. In addition, our definition of PPAT abundance allowed us to identify groups of PCa patients whose PPAT characteristics differ in their histology, transcriptomes and proteomes, paving the way to understand how abundant PPAT promotes PCa progression.

We find that abundant PPAT expands by adipocyte hypertrophy rather than hyperplasia. This hypertrophy may be explained by several mechanisms: the increased expression of lipid transporters involved in uptake of lipids into adipocytes and transport within the cells and the decreased expression of some proteins involved in lipolysis, favoring lipid uptake over degradation. Also, the adipocyte hypertrophy may be facilitated by loss of collagen fibrils from the ECM, which we saw in abundant PPAT, since fibrosis plays a central role in limiting the expandability of AT (Sun et al., 2013) by generating a mechanical stress on hypertrophic adipocytes. Our previous study of PPAT in obesity supports this explanation. We found that lean PPAT has a peculiar vascularization that causes a chronic state of hypoxia leading to fibrosis, this fibrosis preventing PPAT expansion in obese patients (Roumiguié et al., 2022). Thus decreasing this fibrosis is an essential step for PPAT expansion. This discovery that the abundant PPAT contains a loose meshwork of both fibrillar and non-fibrillar collagens is perhaps the most important finding from this study because it explains how the tissue expands without becoming inflamed and the mechanism whereby PPAT expansion promotes PCa aggressivity.

The expansion of PPAT we observe in PCa patients in our high PPAT group does not result in tissue inflammation or in adipocyte dysfunction. This is surprising because expansion of other ATs by hypertrophy, as in obesity, leads to increased local inflammation and changes in the secretory profile of adipocytes (Ouchi et al., 2011). We explain this finding by the loose meshwork of fibrillar and non-fibrillar collagens in high PPAT resulting from enhanced ECM degradation that decrease the expression of proteins involved in mechano-transduction and stiffness sensing. This expansion in a context of decreased mechanical constraints led to a "stress-free" expansion. This loss of mechanical constraints allows the adipocytes to enlarge without cell death, which prevents accumulation of macrophages and, subsequently, in the reduction of the inflammatory microenvironment (Sun et al., 2013; Pellegrinelli et al., 2016). Evidence from mouse models deficient in ECM or overexpressing ECM remodeling proteins, support our interpretation that the loss of mechanical constraints allows PPAT expansion without inflammation. Mice that lack COLVI and that are obese due either to a high fat diet or to *ob/ob* mutation have impaired ECM stability and, hence, reduced AT fibrosis resulting in adipocyte hypertrophy in the absence of inflammation (Khan et al., 2009). Similarly, in a inducible AT specific MMP14 overexpression

model, the overexpression of MMP14 during the early stage of high fat diet (HFD) reduced inflammation and fibrosis (Li et al., 2020). In both cases, this phenotype was linked to the decrease in ECM stiffness of AT, thereby releasing the mechanical stress to allow for its healthy expansion (Khan et al., 2009; Chun et al., 2010).

One of the main differences we saw between the ECM in the high and low PPAT groups was in COLVI, the most abundant non-fibrillar collagen in AT (Sun et al., 2013). Whereas COLVI staining revealed a typical beaded filament network (Cescon et al., 2015) in the PPAT of the low PPAT group, in the high PPAT group the staining was weak and punctiform and the filament network was disorganized. COLVI interacts with many ECM proteins, including fibronectin and collagen types I, II and IV, bridging cells to the surrounding connective tissue and organizing the three-dimensional tissue architecture (Cescon et al., 2015). Thus, the overall loss of collagen may result from initial extensive degradation of COLVI. This degradation probably involves MMP9, which we found was much more abundant in the high PPAT group than in the low PPAT group. Degradation of COLVI by MMP9 has been described previously (Veidal et al., 2011), as well as by MMP2 (Veidal et al., 2011), MMP-11 (Motrescu et al., 2008) and MMP14 (Li et al., 2020). Expression of the latter MMPs and the inhibitors TIMP 1-4 were similar in both groups, however, suggesting that MMP9 is the most important in degrading COLVI in abundant PPAT. We do not know yet what initiates ECM remodeling to allow PPAT to expand. The correlation between the volume of PPAT and the volume of the prostate suggests that steroid hormones might be involved. Consistent with this, MMP9 expression is regulated by androgens (Tang et al., 2021) and sex hormones influence the metabolism, endocrine functions and angiogenesis of certain other ATs (Karastergiou et al., 2012), so this hypothesis deserves further investigation.

We postulate that the extensive ECM remodeling we observe in abundant PPAT promotes PCa aggressivity by producing signaling molecules that act on the adjacent tumor. Enzymatic cleavage of ECM proteins, proteoglycans and glycosaminoglycans produces matrikines and matricryptins, which are active in several biological processes including cancer progression (Ricard-Blum and Salza, 2014). We investigated the role of endotrophin , a matrikine derived from proteolytic cleavage of the carboxy-terminal C5 domain of the COLVI α3 chain from the parental COLVI microfibrils during secretion (Park and Scherer, 2012; Lamandé et al., 2006), because of the substantial amounts of COLVI degradation in abundant PPAT. Also, adipocyte-derived endotrophin favors breast tumor progression and resistance to therapy in genetically engineered mice (Park and Scherer, 2012) and in xenografted human tumors (Bu et al., 2019). Endotrophin targets not only the tumor cells but also induces changes in the tumor stroma including fibrosis, angiogenesis and recruitment of immune cells (Park and Scherer, 2012; Park et al., 2013) by acting directly on several cellular components of the tumor microenvironment (Bu et al., 2019). *In vitro*, endotrophin promotes recruitment and migration of macrophages, proliferation and

branching of endothelial cells, and differentiation of fibroblasts into myofibroblasts (Bu et al., 2019). The tumor microenvironment in PCa patients with abundant PPAT that we report here recapitulates all the features previously shown to be promoted by endotrophin. Moreover, we found more endotrophin in the PPAT of patients in the high PPAT group than in those in the low PPAT group. We found elevated levels specifically of *MMP9* mRNA, MMP9 protein and activity in abundant PPAT. This is consistent with a report that *in vitro* MMP9 activity, along with MMP2 and MMP16, is key to produce active endotrophin (Jo et al., 2022), which might explain the high levels of this matrikine in abundant PPAT. At first sight, our findings appear to contradict those of a study that used inducible adipocyte-specific endotrophin overexpression, which found that endotrophin amplifies AT dysfunction in obesity by enhancing fibrosis and inflammation leading, ultimately, to increased insulin resistance (Sun et al., 2014). In this case, however, endotrophin was overexpressed in the context of obesity-induced fibrosis; it might be considered as a co-stimulator of this pathological condition. In abundant PPAT, by contrast, natural expression of endotrophin occurs in the context of ECM degradation.

At the moment, we have no direct evidence that endotrophin produced in the ECM of PPAT is responsible for the increase in PCa aggressiveness. Such direct evidence would require a mouse model; currently, no mouse model reproduces the abnormal expansion of PPAT. To develop a model, we would need to identify the signal that drives PPAT expansion. Also, since mouse and human prostates differ in their morphology and architecture (Oliveira et al., 2016), it is far from certain that the phenomenon we report in human would be reproduced in mice. We tried to xenograft PPAT from patients in our low PPAT and high PPAT groups close to the prostate glands of immunodeficient mice, but the tissue did not remain viable and functional for long enough to perform experiments (data not shown). Co-culture of primary PPAT explants with prostate cancer cells might be an alternative approach but previous attempts (as well as our own experiments) found rapid adipocyte dedifferentiation associated with an increase in pro-inflammatory cytokines, rendering this approach unsuitable (Gesta et al., 2003) (data not shown).

In addition to the fact that both tumors and their microenvironment in PCa patients with abundant PPAT recapitulates all the features previously shown to be promoted by endotrophin, we show that endotrophin levels are elevated in the urine of patients with abundant PPAT collected after prostate massage, thus validating the clinical relevance of our findings. Endotrophin is stable in biological fluids and serum endotrophin was previously described as a surrogate marker of disease progression in chronic fibrotic and inflammatory diseases such as diabetes, heart failure, kidney disease and liver fibrosis (Rasmussen et al., 2017; Fenton et al., 2017; Leeming et al., 2021) (for review (Williams et al., 2022). We saw no difference between the plasma levels of endotrophin in patients from high and low PPAT groups. In cancer, endotrophin acts locally and its increase in urine reflects escape from the

tumors and their environment. Therefore, measurement of endotrophin after prostate massage might be used to investigate the relationship between PPAT abundance/ECM remodeling and PCa progression in large cohort of patients including those undergoing treatments other than prostatectomy. Our new and robust definition of PPAT abundance can be applied to future translational studies and, potentially, to clinical practice to improve risk stratification. At current time, the use of accepted PCa risk stratification groups based on prostate-specific antigen, clinical stagging (T stage) and Gleason score assists in clinical decision making, clinical trial design and outcomes reporting. Factors from the tumor microenvironment are not considered. Since mpMRI is now widely used prior to biopsies, dedicated clinical trials should be design to assess the interest of PPAT abundance in improving current classification. In addition, our study shows that endotrophin is a good candidate biomarker and a potential pharmacological target to dampen PCa progression. Finally, knowledge of the mechanism(s) that initiate PPAT expansion might allow clinicians to identify preventive approaches to decrease PPAT abundance in order to improve the outcome of PCa patients.

Materials and Methods

Patients, prostate and fat measurements

Between September 2016 and July 2021, patients with localized PCa diagnosed by prostate biopsies who were opting for RP were recruited. We excluded from the study patients with metastatic PCa (as assessed by computerized tomography and/or bone scan), and patients who had received radiotherapy, hormonal or high intensity ultrasound treatment. The study was conducted in accordance with the guidelines and with the full approval of the national ethics committee (AC-2020-4031). Written informed consent was received from participants before inclusion in the study, which was conducted in accordance with the Declaration of Helsinki principles as revised in 2000.

All the patients underwent pre-operative 1.5 T mpMRI after injection with 20 mg of butyl scopolamine (Buscopan; Boehringer-Ingelheim, Paris, France). Anatomic 3D fast spin echo T2-weighted MRI, functional diffusion-weighted MRI and dynamic contrast-enhanced MRI data were acquired. After anonymization of the mpMRI data obtained from the medical records of the patients, the PPAT and prostate volume, the subcutaneous and perirectal AT area were measured by using a semi-automated segmentation technique on contiguous 3 mm T2-weighted axial slices and Olea Sphere software (Olea medical, La Ciotat, France). The subcutaneous AT area was determined by measuring the perpendicular distance between the skin and the anterior upper border of the symphysis pubis on a selected T2-weighted axial slice where it was maximum. The perirectal AT area was determined by segmenting the fat around the rectum at the level of the apex of the prostate. (Table S1). Twenty patients who underwent MRI for suspected PCa with negative results were included in this radiological study for the measure of PPAT and prostate volume (named patients no cancer). One observer, trained by a senior experienced radiologist and blind to the clinical and pathological data, carried out all segmentations and measurements. The PPAT was segmented from the level of the prostate base to the apex (see Figure 1A) (mean 14 slices per patient). The following anatomical boundaries were used to define PPAT limits on each slice: pubic symphysis at the front, obturator muscles on the lateral sides and Denonvilliers fascia at the back (as previously described (Roumiguié et al., 2022). Baseline demographic characteristics (age and BMI), serum Prostate Specific Antigen (PSA) concentration, pathological parameters of the tumor on RP pieces including the volume of the tumor, Gleason score and ISUP group (histological score reflecting the differentiation of PCa determined by a trained pathologist according the 2016 WHO classification and ISUP recommendations), percentage of undifferentiated cancer cells (defined as the percentage of the tumor with a Gleason score greater than 4), pT (pathological T) stage and extraprostatic extension were acquired from the medical records of the patients. The clinical characteristics of the cohort is presented in Table S2. The Gleason score and ISUP group was also determined on pre-operative biopsies by a trained pathologist.

PPAT collection and tissue processing

PPAT from patients undergoing RP were removed and the samples were anonymized. Charred samples and those weighing < 300 mg were excluded from the study. Samples were immediately put in 50 mL tubes containing 10 mL of Dulbecco's Modified Eagle's Medium (DMEM, Thermofischer scientific, Courtaboeuf, France) and were transported to the research lab within 1 h. The samples were weighed and use for several preparations. For RT-qPCR analysis, measure of MMP9 activity and dosage of hydroxyproline content, PPAT were immediately frozen in liquid nitrogen and stored at -80°C for later use. For 3D microscopy, samples were fixed with 4% paraformaldehyde solution at room temperature (RT) for 24 h. Some of the samples were also used to isolate adipocytes and the stromal vascular fraction after collagenase digestion (see below). Finally, samples were used to prepare PPAT-conditioned medium as previously described (Roumiguié et al., 2022). Briefly, 1 g of tissue was incubated overnight in 8 mL of DMEM supplemented with 1% BSA in a humidified incubator at 37°C and with 5% CO_2 and the medium was collected after filtration through a 0.2 μM filter. The conditioned media were immediately stored in small aliquots at -80°C.

Histology and immunohistochemistry

A part of the PPAT sample was sent along with the resected tumor to the Pathology Department and both tissues were embedded in paraffin. Prior staining, PPAT or tumor sections (3 μm) were deparaffinized with xylene for 5 min, dehydrated in 100% alcohol for 5 min, and then rehydrated in running tap water for 10 min. The PPATs were stained with HE as previously described (Roumiguié et al., 2022). For Masson Trichrome staining (MAST), the tumor sections were first stained in Mayer's hemalum solution for 20 min and washed in distilled water and in ammonia water each for 30 s. Then they were stained in Ponceau S solution for 1 min and washed in distilled water. They were differentiated in 1% phosphomolybdic solution for 5 min, transferred to aniline blue solution and stained for a further 5 min. The tissues were rinsed briefly in distilled water and differentiated in 1% acetic acid solution for 4 min, then dehydrated rapidly through alcohol and cleared in xylene. Automated classical immunohistochemical (IHC) stain was performed using the Benchmark ULTRA (Roche, Ventana Medical Systems, Arizona, USA) on formalin-fixed paraffin-embedded tumor sections (3 μm). After dewaxing, tissue slides were heat pre-treated using a Cell Conditioning Buffer 1 (pH 8) (Roche Diagnostic, Meylan, France) at 98°C. The slides were blocked for endogenous peroxidase activity and incubated with primary anti-CD31 (Clone JC70, (ready to use), Roche Diagnostics, Meylan, France) or anti-CD68 (clone PGM1, dilution 1/100, Agilent Technologies, Les Ulis, France) antibody. The target was then visualized using the OptiView DAB detection kit (Roche Diagnostic, Meylan, France). The tissue slides were counterstained using hematoxylin (Roche Diagnostic, Meylan, France) for 8 min

followed by post-coloration using Bluing reagent for 4 min at RT (Roche Diagnostic, Meylan, France). The slides were then dehydrated (ethanol and xylene) and mounted using xylene-based mounting.
Tumor staining (i.e. MAST, CD31 and CD68) was quantified on 20 images at 20x magnification taken randomly for each tumor using ImageJ (v1.56.j). Color deconvolution was applied on RGB images to extract MAST or DAB specific signals which were quantified and normalized to the tissue area determined from source images. The mean diameter of adipocytes was determined using Adiposoft software a plugin of Image J (v1.56.j) as previously described (Roumiguié et al., 2022).

Isolation of AT stromal vascular fraction (SVF) and mature adipocytes

Digestion of fresh PPAT was performed as previously described (Roumiguié et al., 2022). Briefly, PPAT were digested with 250 U/ml type I collagenase (Sigma-Aldrich, Saint-Quentin-Fallavier, France) in PBS containing 2 % BSA for 30 min at 37°C under constant shaking. The samples were filtered with a 250 µm cell strainers and the cell suspensions were then gently centrifuged for 1 min at 20 g at RT to pack adipocytes on the top layer. Floating adipocytes were collected and rinsed with KRB buffer supplemented with 1mM Hepes and 0.5% FFA free-BSA (all obtained from Sigma-Aldrich, Saint-Quentin-Fallavier, France) to obtain pure adipocyte cell suspensions that were used for proteomic analysis (see below). After removal of adipocytes, the remaining cell suspension was centrifuged at 300 g for 10 min to pellet SVF cells. Erythrocytes were lysed by incubation at RT in erythrocyte lysis buffer (155 mM NH_4Cl, 5.7 mM K2HPO4, 0.1 mM EDTA, pH 7.3) for 10 min followed by successive filtration through 100, 70, and 40 µm strainers. The viable recovered cells were washed 2 times in PBS, counted and analyzed by flow cytometry.

Flow cytometry analysis

Flow cytometry was performed as previously described with minor modifications (Estève et al., 2019). Briefly, 100 000 stromal vascular cells were incubated for 30 min at 4 °C in PBS supplemented with 0.5% BSA and 2 mM EDTA containing fluorescently labeled antibodies. Brilliant Violet 510™ anti-human CD45 (clone HI30, dilution 1/20, Biolegend, Amsterdam, The Netherlands), APC anti-human CD206 (clone 19.2, dilution 1/10, BD Biosciences, Le Pont de Claix, France) and PE-Vio® 770 anti-human CD14 (clone TÜK4, dilution 1/50, Miltenyi Biotec, Paris, France) antibodies were used for macrophages phenotyping. PerCP anti-human CD34 (Clone 8G12, dilution 1/20, BD Biosciences, Le Pont de Claix, France), BV450 anti-human CD31 (Clone WM59, dilution 1/20, BD Biosciences, Le Pont de Claix, France), PE anti-human MSCA1 (Clone W8B2, dilution 1/10, Miltenyi Biotec, Paris, France), APC anti-human CD271 (Clone ME20.4-1.H4, dilution 1/10, Miltenyi Biotec, Paris, France) and Brilliant Violet 510™ anti-human CD45 (clone HI30, dilution 1/20, Biolegend, Amsterdam, The Netherlands) antibodies

were used for progenitor cell subset phenotyping. Brilliant Violet 510™ anti-human CD45 (clone HI30, dilution 1/20, Biolegend, Amsterdam, the Netherlands), Brilliant Violet 450 anti-human CD3 (Clone UCHT1, dilution 1/20, BD Biosciences, Le Pont de Claix, France), FITC anti-human CD4 (Clone RPA-T4, dilution 1/20, BD Biosciences, Le Pont de Claix, France), PerCP anti-human CD8 (Clone SK1, dilution 1/10, BD Biosciences, Le Pont de Claix, France) and APC anti-human CD25 (Clone 2A3, dilution 1/10, BD Biosciences, Le Pont de Claix, France) antibodies were used for lymphocyte phenotyping. As control, a panel of appropriate isotype antibodies was used. The labeled cells were washed with PBS and analyzed in a FACS Canto™ II flow cytometer using Diva Pro software (BD Biosciences, Le Pont de Claix, France). Cell debris, dead cells and doublets were excluded based on scatter signals. Compensation was established using compensation particles set (BD Biosciences, Le Pont de Claix, France) and single staining and flow cytometer calibration was performed with rainbow calibration particles (BD Biosciences, Le Pont de Claix, France).

ELISA assays

As previously described (Roumiguié et al., 2022), a panel of secreted adipokines were quantified in PPAT-CM with an ELISA kit (LXSAHM-08; R&D Systems, Noyal Châtillon sur Seiche, France) and a mixture of antibodies against Adiponectin/Acrp30, IL-6, IL-1β, Leptin, MCP1 and TNFα, according to the protocol provided by the manufacturer. Endotrophin was quantified in plasma and urine collected after prostate massage using homemade ELISA as previously described (Bu et al., 2019).

RNA extraction and RT-qPCR

For RNA extraction, 100 mg of frozen tissue was mixed with 500 µl QIAzol™ lysis reagent (Qiagen, Courtaboeuf, France) and homogenized with a Precellys ® tissue homogenizer (2 cycles of 45 seconds at 7500 rpm at 4°C) using the Cryolys cooling system. The tissue homogenates were centrifuged for 1 min at 5000 g at RT. The lipid-containing surface layer was then removed and 350µl of chloroform was added. The organic and aqueous phases were separated by centrifugation (10 min at 5000 g at RT). The upper phase, containing RNA, was recovered and mixed with ethanol for RNA extraction using the Qiagen RNeasy mini kit as described by the manufacturer (Qiagen, Courtaboeuf, France). The RNA concentration was determined with a Nanodrop 2000 spectrophotometer at a wavelength of 260nm. cDNA were reverse transcribed from 250 ng of purified RNA by using the RevertAid H Minus First Strand cDNA synthesis kit (Thermo Fisher Scientific, Illkirch-Graffenstaden, France) with hexamer random primers according to the supplier's recommendations. Gene expression was quantified by RT-qPCR on 6.25 ng of cDNA with TaqMan primers (the primers used are listed in Table S7), Thermo Fisher Scientific, Illkirch-Graffenstaden, France) and Fast Advanced TaqMan Master Mix (Thermo Fisher

Scientific, Illkirch-Graffenstaden, France) in a final volume of 20 µl with a CFX96real time PCR system (Bio-Rad). Results were normalized to the amount of 18S rRNA.

Sample preparation for proteomic analysis

Isolated adipocytes obtained as described above were washed in PBS three times and proteins were extracted from 500 µl of adipocyte with 500 µl 1X RIPA buffer (Sigma-Aldrich) supplemented with complete antiprotease tablet (Roche) with a precellys tissue homogenizer and Ceramic beads (CK14) with 2 cycles of 45 s at 7500rpm at 4°C. The samples were then centrifuged 10 min at 10 000 g at RT to separate and aggregate the lipids at the top layer from which they were removed. The extract was recovered without the top layer containing the lipids and centrifuged again 10 min at 10 000 g at 4°C. Protein concentration was determined using DC protein assay kit (Biorad, Biorad, Marnes-la-Coquette, France) following manufacturer instructions. 40µg of proteins was digested for proteomic characterization by mass spectrometry using the S-Trap™ micro spin column (ProtiFi, NY USA).

LC-MS/MS analysis.

Tryptic peptides were resuspended in 40 µl of 2% acetonitrile and 0.05% trifluoroacetic acid and analyzed by nano-liquid chromatography using an UltiMate 3000 system (NCS-3500RS Nano/Cap System; Thermo Fisher Scientific) coupled to an Orbitrap Q Exactive HF-X mass spectrometer (Thermo Fisher Scientific). Peptides were separated on an Acclaim PepMap C18 column (id 75 µm, length 50 cm, particle size 2 µm, Thermo Fisher Scientific) using a 10%-45% gradient of solvent B (80% acetonitrile, 0.2% formic acid), over 120 min (solvent A: 5% acetonitrile, 0.2% formic acid). The mass spectrometer was operated in data-dependent acquisition mode with the Xcalibur software.

Bioinformatic MS data analysis: Acquired MS and MS/MS data were searched with Mascot (version 2.6.1, http://matrixscience.com) against the Human UniProtKB database (Swiss-Prot/TrEmbl, 556,568 entries). Cysteine carbamidomethylation was set as a fixed modification. Methionine oxidation and acetylation of protein N-terminus were set as variable modification. Up to two missed trypsin/P cleavages were allowed. Mass tolerances in MS and MS/MS were set to 10 ppm and 0.8 Da, respectively.

Proline software (version 1.6, http://proline.profiproteomics.fr/) was used for the validation of identifications and the label-free quantification of identified proteins (Bouyssié et al., 2020). Mascot identification results were imported into Proline. Search results were validated through a false-discovery rate (FDR) set to 1% at protein and peptide-sequence match level. Proteins with a p-value < 0.05 and a ratio of average normalized area < 0.5 and > 2 were considered significant. Volcano plots were drawn to visualize significant protein abundance variations between two conditions control and assay.

They represent log10 (p-value) according to the log2 ratio. Label free quantification intensities were normalized between samples with the function "NormalizeBetweenArrays" from limma package (v3.40.6) in R (v3.6). Differential analysis was computed with limma package from Bioconductor. Principal component analysis was performed with R (v3.6) and FactoMineR package (v2.4). Go term enrichment analysis was performed with Molecular signature database on differentially represented proteins (V7.4 MSigDB). The mass spectrometry proteomics data have been deposited to the ProteomeXchange Consortium via the PRIDE partner repository with the dataset identifier PXD038514. Reviewer account details: Username: reviewer_pxd038514@ebi.ac.uk; Password: 5QSTgkLK.

3D confocal microscopy and quantification

For immunofluorescence staining, PPAT (250mg) were saturated and permeabilized with PBS supplemented with 3 % BSA and 0.2 % Triton X100 (Sigma-Aldrich, Saint-Quentin-Fallavier, France) for 1 h. Tissues were then incubated overnight at 4°C with the following primary antibodies diluted in PBS 3% BSA 0.2% Triton X100: anti-β-Tubulin (clone 2A1A9, dilution 1/200, Abcam, Cambridge, UK), anti-YAP1 (clone D8H1X, dilution 1/200, Cell Signaling Technology, Leiden, The Netherlands), Anti-Pan Collagen VI (clone 3C4, dilution 1/200, Millipore, Guyancourt, France) and serum anti-human ETP (Bu et al., 2019) (dilution 1/100) antibodies. Tissues were washed 5 times with PBS - 0.05% Tween for 10 min. Then, tissues were incubated with secondary antibodies coupled with fluorescent dye (dilution 1/800, Biotium, Fremont, CA, USA) according to the species in which the primary antibodies were produced for 3h at RT and with or without rhodamine-phalloidin (dilution 1/200, Thermofisher, Waltham, MA, USA) diluted in PBS, 3% BSA and 0.2% Triton X100. Tissues were washed 5 times with PBS 0.05% Tween for 10 min. Nuclei were stained with Hoechst 33342 (dilution 1/1000, Invitrogen, Villebon sur Yvette, France) for 30 min and after 3 washes in PBS Z stack images were acquired using LSM710 confocal microscope and 40X objective. For Fluorescent Collagen Hydridizing Peptides (F-CHP, Cat@FLU-300, Clinisciences, Nanterre,France), fixed AT were incubated with 20µM of F-CHP overnight at 4° C. Tissue were rinsed with PBS 5 times for 5-10 min. Z stack images were acquired using LSM710 confocal microscope and 40X objective. Staining were quantified with Imaris software (v9.2). Briefly, after segmentation and thresholding of the staining of interest, volumes were rendered with the surface module of Imaris. Extracted statistics were normalized to the volume of the tissue determined with the autofluorescence of the tissue.

For Picrosirius Red, fixed AT were incubated for 3 h in Picrosirius Red solution (1 g/L Sirius red in 1.3% picric acid). After two washes in acidified water followed by fixation and dehydration steps in 100% ethanol, images were acquired with a confocal microscope (LSM710, Zeiss International, Oberkochen, Germany) equipped with a 40 oil-immersion inverted objective with a numerical aperture of 1.3. The samples were excited at 560 nm, and fluorescence emission was collected above 580 nm. Pinhole was

setup at 0.7 Airy (ZEN imaging software; Zeiss International) to increase resolution. Three-dimensional reconstructions and analyses of collagen fiber organization were performed with Imaris software and the filament tracer module. The data generated were normalized to the tissue volume obtained after tissue surface reconstruction with Imaris (v9.6) (Bitplane, Gometz la Ville, France).

Hydroxyproline quantification

Fragments of PPAT of about 100 mg were weighed precisely, placed in 500 µl deionized water in a Precellys® 2mL Soft Tissue homogenizing Ceramic beads Kit (CK14) (Ozyme, Saint-Cyr-l'École, France) and extracted by using the Precellys® tissue homogenizer with 2 cycles of 45 seconds at 7500 rpm at RT. Samples were then centrifuged for 10 min at 5000 g at RT to remove lipids floating on the top layer by pipetting. Lipid-free supernatants were vortex mixed, 150 µl were mixed with an equal volume of 10 M NaOH and heated at 105°C for 1 hour to fully digest collagens. The reaction was stopped by adding 150 µl of 10M HCl. Hydroxyproline was quantified in duplicate by using the Hydroxyproline Assay Kit (Perchlorate-Free; Milpitas, CA, USA) as recommended by the supplier and normalized to the precise tissue weight initially digested.

MMP9 activity

For protein extraction, 100-250 mg of frozen tissues were incubated with 400 µl of RIPA lysis buffer (Sigma-Aldrich, Saint-Quentin-Fallavier, France). Proteins were extracted using the Precellys ® tissue homogenizer and Soft Tissue homogenizing Ceramic beads (CK14) with 2 cycles of 45 seconds at 7500 rpm at RT. The samples were then centrifuged 10 min at 5000 g at RT to separate and aggregate the lipids on the top layer. The lipid-free phase was recovered, sonicated and centrifuged again 10 min at 10 000 g at 4°C. Protein concentration was quantified with DC protein assays (Bio Rad, Marnes-la-Coquette, France). Concentration of active MMP9 on 200µg of total proteins lysate was quantified by using a Human Active MMP-9 Fluorokine E assay kit (F9M00; R&D Systems, Noyal Châtillon sur Seiche, France) according to the protocol provided by the manufacturer. Fluorescence was quantified using FLX800 fluorimeter with an excitation wavelength set to 340nm and an emission wavelength set to 405nm.

Statistics

Univariate statistical analysis of clinical data was performed using ANOVA for continuous variables or using Chi square test for qualitative variables with Prism (v5.04). Linear regression was computed with Prism v5.04 and residuals were calculated according to the fitted linear model. Multivariate analysis was performed by multiple logistic regression using the glm function from R (v3.6) to predict patients having an ISUP score above or equal to 3. For experimental data, statistical analysis was performed

using Student T test after testing normality distribution using Kolgomorov-Smirnov test for comparison between two groups or with ANOVA followed by test for linear trends between 3 groups. Statistical differences were considered as significant if the p-value was below 0.05.

Acknowledgements

This work benefited from the Toulouse Réseau Imagerie (TRI)-RIO Optical Imaging Platform at the Institute of Pharmacology and Structural Biology (Genotoul, Toulouse, France). We acknowledge Life Science Editors for professional scientific editing during the preparation of the manuscript.

This study was supported by the Ligue Nationale Contre le Cancer (Équipe Labélisée), the French National Cancer Institute (INCA PL-BIO 2016-176 to AB, BM, PV, and CM), by the Fondation Toulouse Cancer Santé (to AB, BM, OBS, PV and CM) and by the Fondation ARC (Association de Recherche contre le Cancer) Programmes Labelisés 2016 (to AB, PV and CM). The work was also funded in part by the French Ministry of Research with the Investissement d'Avenir Infrastructures Nationales en Biologie et Santé program (ProFI, Proteomics French Infrastructure project, ANR-10-INBS-08) (to OBS). DE received a post-doctoral fellowship from the Fondation pour La Recherche Médicale (SPF201809007124).

References

Bouyssié, D., A.-M. Hesse, E. Mouton-Barbosa, M. Rompais, C. Macron, C. Carapito, A. Gonzalez de Peredo, Y. Couté, V. Dupierris, A. Burel, J.-P. Menetrey, A. Kalaitzakis, J. Poisat, A. Romdhani, O. Burlet-Schiltz, S. Cianférani, J. Garin, and C. Bruley. 2020. Proline: an efficient and user-friendly software suite for large-scale proteomics. *Bioinformatics*. 36:3148–3155. doi:10.1093/bioinformatics/btaa118.

Bu, D., C. Crewe, C.M. Kusminski, R. Gordillo, A.L. Ghaben, M. Kim, J. Park, H. Deng, W. Xiong, X.Z. Liu, P.E. Lønning, N. Halberg, A. Rios, Y. Chang, A. Gonzalez, N. Zhang, Z. An, and P.E. Scherer. 2019. Human endotrophin as a driver of malignant tumor growth. *JCI Insight*. 4. doi:10.1172/jci.insight.125094.

Cao, Y., and J. Ma. 2011. Body mass index, prostate cancer-specific mortality, and biochemical recurrence: A systematic review and meta-analysis. *Cancer Prevention Research*. 4:486–501. doi:10.1158/1940-6207.CAPR-10-0229.

Cescon, M., F. Gattazzo, P. Chen, and P. Bonaldo. 2015. Collagen VI at a glance. *Journal of Cell Science*. 128:3525–3531. doi:10.1242/jcs.169748.

Chun, T.H., M. Inoue, H. Morisaki, I. Yamanaka, Y. Miyamoto, T. Okamura, K. Sato-Kusubata, and S.J. Weiss. 2010. Genetic link between obesity and MMP14-dependent adipogenic collagen turnover. *Diabetes*. 59:2484–2494. doi:10.2337/db10-0073.

Costello, A.J. 2020. Considering the role of radical prostatectomy in 21st century prostate cancer care. *Nature Reviews Urology*. 17:177–188. doi:10.1038/s41585-020-0287-y.

Dahran, N., M. Szewczyk-Bieda, S. Vinnicombe, S. Fleming, and G. Nabi. 2019. Periprostatic fat adipokine expression is correlated with prostate cancer aggressiveness in men undergoing radical prostatectomy for clinically localized disease. *BJU International*. 123:985–994. doi:10.1111/bju.14469.

Dahran, N., M. Szewczyk-Bieda, C. Wei, S. Vinnicombe, and G. Nabi. 2017. Normalized periprostatic fat MRI measurements can predict prostate cancer aggressiveness in men undergoing radical prostatectomy for clinically localised disease article. *Scientific Reports*. 7. doi:10.1038/s41598-017-04951-8.

Dupont, S., L. Morsut, M. Aragona, E. Enzo, S. Giulitti, M. Cordenonsi, F. Zanconato, J. Le Digabel, M. Forcato, S. Bicciato, N. Elvassore, and S. Piccolo. 2011. Role of YAP/TAZ in mechanotransduction. *Nature*. 474:179–184. doi:10.1038/nature10137.

Estève, D., N. Boulet, C. Belles, A. Zakaroff-Girard, P. Decaunes, A. Briot, Y. Veeranagouda, M. Didier, A. Remaury, J.C. Guillemot, S. Ledoux, C. Dani, A. Bouloumié, and J. Galitzky. 2019. Lobular architecture of human adipose tissue defines the niche and fate of progenitor cells. *Nature Communications*. 10. doi:10.1038/s41467-019-09992-3.

Estève, D., M. Roumiguié, C. Manceau, D. Milhas, and C. Muller. 2020. Periprostatic adipose tissue: A heavy player in prostate cancer progression. *Current Opinion in Endocrine and Metabolic Research*. 10:29–35. doi:10.1016/j.coemr.2020.02.007.

Fenton, A., M.D. Jesky, C.J. Ferro, J. Sørensen, M.A. Karsdal, P. Cockwell, and F. Genovese. 2017. Serum endotrophin, a type VI collagen cleavage product, is associated with increased mortality in chronic kidney disease. *PLoS ONE*. 12. doi:10.1371/journal.pone.0175200.

Frühbeck, G., V. Catalán, A. Rodríguez, B. Ramírez, S. Becerril, J. Salvador, I. Colina, and J. Gómez-Ambrosi. 2019. Adiponectin-leptin ratio is a functional biomarker of adipose tissue inflammation. *Nutrients*. 11. doi:10.3390/nu11020454.

Fujita, K., and N. Nonomura. 2018. Urinary biomarkers of prostate cancer. *International Journal of Urology*. 25:770–779. doi:10.1111/iju.13734.

Funcke, J.B., and P.E. Scherer. 2019. Beyond adiponectin and leptin: Adipose tissue-derived mediators of inter-organ communication. *Journal of Lipid Research*. 60:1648–1697. doi:10.1194/jlr.R094060.

Gesta, S., K. Lolmède, D. Daviaud, M. Berlan, A. Bouloumié, M. Lafontan, P. Valet, and J.S. Saulnier-Blache. 2003. Culture of Human Adipose Tissue Explants Leads to Profound Alteration of Adipocyte Gene Expression. *Horm Metab Res*. 35:158–163. doi:10.1055/s-2003-39070.

Gregg, J.R., D.S. Surasi, A. Childs, N. Moll, J.F. Ward, J. Kim, C.R. Daniel, C. Logothetis, T. Bathala, and J.W. Davis. 2021. The Association of Periprostatic Fat and Grade Group Progression in Men with Localized Prostate Cancer on Active Surveillance. *The Journal of urology*. 205:122–128. doi:10.1097/JU.0000000000001321.

Gucalp, A., N.M. Iyengar, X.K. Zhou, D.D. Giri, D.J. Falcone, H. Wang, S. Williams, M.D. Krasne, I. Yaghnam, B. Kunzel, P.G. Morris, L.W. Jones, M. Pollak, V.P. Laudone, C.A. Hudis, H.I. Scher, P.T. Scardino, J.A. Eastham, and A.J. Dannenberg. 2017. Periprostatic adipose inflammation is associated with high-grade prostate cancer. *Prostate Cancer and Prostatic Diseases*. 20:418–423. doi:10.1038/pcan.2017.31.

Harrison, S., K. Tilling, E.L. Turner, R.M. Martin, R. Lennon, J.A. Lane, J.L. Donovan, F.C. Hamdy, D.E. Neal, J.L.H.R. Bosch, and H.E. Jones. 2020. Systematic review and meta-analysis of the associations between body mass index, prostate cancer, advanced prostate cancer, and prostate-specific antigen. *Cancer Causes and Control*. 31:431–449. doi:10.1007/s10552-020-01291-3.

Huang, H., S. Chen, W. Li, P. Bai, X. Wu, and J. Xing. 2019. Periprostatic Fat Thickness on MRI is an Independent Predictor of Time to Castration-resistant Prostate Cancer in Chinese Patients With Newly Diagnosed Prostate Cancer Treated With Androgen Deprivation Therapy. *Clinical Genitourinary Cancer*. 17:e1036–e1047. doi:10.1016/j.clgc.2019.06.001.

Hwang, J., Y. Huang, T.J. Burwell, N.C. Peterson, J. Connor, S.J. Weiss, S.M. Yu, and Y. Li. 2017. In Situ Imaging of Tissue Remodeling with Collagen Hybridizing Peptides. *ACS Nano*. 11:9825–9835. doi:10.1021/acsnano.7b03150.

Ichikawa, T., M. Kita, T.S. Matsui, A.I. Nagasato, T. Araki, S.H. Chiang, T. Sezaki, Y. Kimura, K. Ueda, S. Deguchi, A.R. Saltiel, and N. Kioka. 2017. Vinexin family (SORBS) proteins play different roles in stiffnesssensing and contractile force generation. *Journal of Cell Science*. 130:3517–3531. doi:10.1242/jcs.200691.

Jo, W., M. Kim, J. Oh, C.-S. Kim, C. Park, S. Yoon, C. Lee, S. Kim, D. Nam, and J. Park. 2022. MicroRNA-29 Ameliorates Fibro-Inflammation and Insulin Resistance in HIF1α-Deficient Obese Adipose Tissue by Inhibiting Endotrophin Generation. *Diabetes*. 71:1746–1762. doi:10.2337/db21-0801.

Kapoor, J., B. Namdarian, J. Pedersen, C. Hovens, D. Moon, J. Peters, A.J. Costello, P. Ruljancich, and N.M. Corcoran. 2013. Extraprostatic extension into periprostatic fat is a more important determinant of prostate cancer recurrence than an invasive phenotype. *Journal of Urology*. 190:2061–2067. doi:10.1016/j.juro.2013.06.050.

Karastergiou, K., S.R. Smith, A.S. Greenberg, and S.K. Fried. 2012. Sex differences in human adipose tissues - The biology of pear shape. *Biology of Sex Differences*. 3. doi:10.1186/2042-6410-3-13.

Khan, T., E.S. Muise, P. Iyengar, Z. V. Wang, M. Chandalia, N. Abate, B.B. Zhang, P. Bonaldo, S. Chua, and P.E. Scherer. 2009. Metabolic Dysregulation and Adipose Tissue Fibrosis: Role of Collagen VI. *Molecular and Cellular Biology*. 29:1575–1591. doi:10.1128/mcb.01300-08.

Lamandé, S.R., M. Mörgelin, N.E. Adams, C. Selan, and J.M. Allen. 2006. The C5 domain of the collagen VI α3(VI) chain is critical for extracellular microfibril formation and is present in the extracellular matrix of cultured cells. *Journal of Biological Chemistry*. 281:16607–16614. doi:10.1074/jbc.M510192200.

Laurent, V., A. Guérard, C. Mazerolles, S. Le Gonidec, A. Toulet, L. Nieto, F. Zaidi, B. Majed, D. Garandeau, Y. Socrier, M. Golzio, T. Cadoudal, K. Chaoui, C. Dray, B. Monsarrat, O. Schiltz, Y.Y. Wang, B. Couderc, P. Valet, B. Malavaud, and C. Muller. 2016. Periprostatic adipocytes act as a driving force for prostate cancer progression in obesity. *Nature Communications*. 7. doi:10.1038/ncomms10230.

Laurent, V., A. Toulet, C. Attané, D. Milhas, S. Dauvillier, F. Zaidi, E. Clement, M. Cinato, S. Le Gonidec, A. Guérard, C. Lehuédé, D. Garandeau, L. Nieto, E. Renaud-Gabardos, A.C. Prats, P. Valet, B. Malavaud, and C. Muller. 2019. Periprostatic adipose tissue favors prostate cancer cell invasion in an obesity-dependent manner: Role of oxidative stress. *Molecular Cancer Research*. 17:821–835. doi:10.1158/1541-7786.MCR-18-0748.

Leeming, D.J., S.H. Nielsen, R. Vongsuvanh, P. Uchila, M.J. Nielsen, A.L. Reese-Petersen, D. van der Poorten, M. Eslam, D. Schuppan, M.A. Karsdal, and J. George. 2021. Endotrophin, a pro-peptide of Type VI collagen, is a biomarker of survival in cirrhotic patients with hepatocellular carcinoma. *Hepatic Oncology*. 8. doi:10.2217/hep-2020-0030.

Li, X., Y. Zhao, C. Chen, L. Yang, H. Lee, Z. Wang, N. Zhang, M.G. Kolonin, Z. An, X. Ge, P.E. Scherer, and K. Sun. 2020. Critical Role of Matrix Metalloproteinase 14 in Adipose Tissue Remodeling during Obesity. *Molecular and Cellular Biology*. 40. doi:10.1128/MCB.00564-19.

Loeb, S., A. Kettermann, H.B. Carter, L. Ferrucci, E.J. Metter, and P.C. Walsh. 2009. Prostate Volume Changes Over Time: Results From the Baltimore Longitudinal Study of Aging. *Journal of Urology*. 182:1458–1462. doi:10.1016/j.juro.2009.06.047.

Ma, B., H. Cheng, R. Gao, C. Mu, L. Chen, S. Wu, Q. Chen, and Y. Zhu. 2016. Zyxin-Siah2-Lats2 axis mediates cooperation between Hippo and TGF-β signalling pathways. *Nature Communications*. 7. doi:10.1038/ncomms11123.

Motrescu, E.R., S. Blaise, N. Etique, N. Messaddeq, M.P. Chenard, I. Stoll, C. Tomasetto, and M.C. Rio. 2008. Matrix metalloproteinase-11/stromelysin-3 exhibits collagenolytic function against collagen VI under normal and malignant conditions. *Oncogene*. 27:6347–6355. doi:10.1038/onc.2008.218.

Nassar, Z.D., A.T. Aref, D. Miladinovic, C.Y. Mah, G.V. Raj, A.J. Hoy, and L.M. Butler. 2018. Peri-prostatic adipose tissue: the metabolic microenvironment of prostate cancer. *BJU International*. 121:9–21. doi:10.1111/bju.14173.

Oliveira, D.S.M., S. Dzinic, A.I. Bonfil, A.D. Saliganan, S. Sheng, and R.D. Bonfil. 2016. The mouse prostate: A basic anatomical and histological guideline. *Bosnian Journal of Basic Medical Sciences*. 16:8–13. doi:10.17305/bjbms.2016.917.

Ouchi, N., J.L. Parker, J.J. Lugus, and K. Walsh. 2011. Adipokines in inflammation and metabolic disease. *Nature Reviews Immunology*. 11:85–97. doi:10.1038/nri2921.

Park, J., T.S. Morley, and P.E. Scherer. 2013. Inhibition of endotrophin, a cleavage product of collagen VI, confers cisplatin sensitivity to tumours. *EMBO Molecular Medicine*. 5:935–948. doi:10.1002/emmm.201202006.

Park, J., and P.E. Scherer. 2012. Adipocyte-derived endotrophin promotes malignant tumor progression. *Journal of Clinical Investigation*. 122:4243–4256. doi:10.1172/JCI63930.

Pellegrinelli, V., S. Carobbio, and A. Vidal-Puig. 2016. Adipose tissue plasticity: how fat depots respond differently to pathophysiological cues. *Diabetologia*. 59:1075–1088. doi:10.1007/s00125-016-3933-4.

Pernar, C.H., E.M. Ebot, K.M. Wilson, and L.A. Mucci. 2018. The epidemiology of prostate cancer. *Cold Spring Harbor Perspectives in Medicine*. 8. doi:10.1101/CSHPERSPECT.A030361.

Rasmussen, D.G.K., A. Fenton, M. Jesky, C. Ferro, P. Boor, M. Tepel, M.A. Karsdal, F. Genovese, and P. Cockwell. 2017. Urinary endotrophin predicts disease progression in patients with chronic kidney disease. *Scientific Reports*. 7. doi:10.1038/s41598-017-17470-3.

Rausch, V., and C.G. Hansen. 2020. The Hippo Pathway, YAP/TAZ, and the Plasma Membrane. *Trends in Cell Biology*. 30:32–48. doi:10.1016/j.tcb.2019.10.005.

Ricard-Blum, S., and R. Salza. 2014. Matricryptins and matrikines: Biologically active fragments of the extracellular matrix. *Experimental Dermatology*. 23:457–463. doi:10.1111/exd.12435.

Van Roermund, J.G.H., K.A. Hinnen, C.J. Tolman, G.H. Bol, J.A. Witjes, J.L.H.R. Bosch, L.A. Kiemeney, and M. Van Vulpen. 2011. Periprostatic fat correlates with tumour aggressiveness in prostate cancer patients. *BJU International*. 107:1775–1779. doi:10.1111/j.1464-410X.2010.09811.x.

Roumiguié, M., D. Estève, C. Manceau, A. Toulet, J. Gilleron, C. Belles, Y. Jia, C. Houël, S. Pericart, S. LeGonidec, P. Valet, M. Cormont, J.-F. Tanti, B. Malavaud, A. Bouloumié, D. Milhas, and C. Muller. 2022. Periprostatic adipose tissue displays a chronic hypoxic state that limits its expandability. *The American Journal of Pathology*. doi:10.1016/j.ajpath.2022.03.008.

Salji, M., J. Hendry, A. Patel, I. Ahmad, C. Nixon, and H.Y. Leung. 2018. Peri-prostatic Fat Volume Measurement as a Predictive Tool for Castration Resistance in Advanced Prostate Cancer. *European Urology Focus*. 4:858–866. doi:10.1016/j.euf.2017.01.019.

Sasaki, T., Y. Sugino, M. Kato, K. Nishikawa, and H. Kanda. 2020. Pre-treatment ratio of periprostatic to subcutaneous fat thickness on MRI is an independent survival predictor in hormone-naïve men with advanced prostate cancer. *International Journal of Clinical Oncology*. 25:370–376. doi:10.1007/s10147-019-01559-y.

Shiao, S.L., G.C.Y. Chu, and L.W.K. Chung. 2016. Regulation of prostate cancer progression by the tumor microenvironment. *Cancer Letters*. 380:340–348. doi:10.1016/j.canlet.2015.12.022.

Sun, K., J. Park, O.T. Gupta, W.L. Holland, P. Auerbach, N. Zhang, R. Goncalves Marangoni, S.M. Nicoloro, M.P. Czech, J. Varga, T. Ploug, Z. An, and P.E. Scherer. 2014. Endotrophin triggers adipose tissue fibrosis and metabolic dysfunction. *Nature communications*. 5:3485. doi:10.1038/ncomms4485.

Sun, K., J. Tordjman, K. Clément, and P.E. Scherer. 2013. Fibrosis and adipose tissue dysfunction. *Cell Metabolism*. 18:470–477. doi:10.1016/j.cmet.2013.06.016.

Tan, W.P., C. Lin, M. Chen, and L.A. Deane. 2016. Periprostatic Fat: A Risk Factor for Prostate Cancer? *Urology*. 98:107–112. doi:10.1016/j.urology.2016.07.042.

Tang, Q., B. Cheng, R. Dai, and R. Wang. 2021. The Role of Androgen Receptor in Cross Talk Between Stromal Cells and Prostate Cancer Epithelial Cells. *Frontiers in Cell and Developmental Biology*. 9. doi:10.3389/fcell.2021.729498.

Veidal, S.S., M.A. Karsdal, E. Vassiliadis, A. Nawrocki, M.R. Larsen, Q.H.T. Nguyen, P. Hägglund, Y. Luo, Q. Zheng, B. Vainer, and D.J. Leeming. 2011. MMP mediated degradation of type VI collagen is highly associated with liver Fibrosis - Identification and validation of a novel biochemical marker assay. *PLoS ONE*. 6. doi:10.1371/journal.pone.0024753.

Wang, J., and W. Pan. 2020. The biological role of the collagen alpha-3 (Vi) chain and its cleaved c5 domain fragment endotrophin in cancer. *OncoTargets and Therapy*. 13:5779–5793. doi:10.2147/OTT.S256654.

Williams, L., T. Layton, N. Yang, M. Feldmann, and J. Nanchahal. 2022. Collagen VI as a driver and disease biomarker in human fibrosis. *FEBS Journal*. 289:3603–3629. doi:10.1111/febs.16039.

Woo, S., J.Y. eon Cho, S.Y. oun Kim, and S.H. yup Kim. 2015. Periprostatic fat thickness on MRI: correlation with Gleason score in prostate cancer. *AJR. American journal of roentgenology*. 204:W43–W7. doi:10.2214/AJR.14.12689.

Zhai, L., Y. Fan, S. Sun, H. Wang, Y. Meng, S. Hu, X. Wang, W. Yu, and J. Jin. 2018. PI-RADS v2 and periprostatic fat measured on multiparametric magnetic resonance imaging can predict upgrading in radical prostatectomy pathology amongst patients with biopsy Gleason score 3 + 3 prostate cancer. *Scandinavian Journal of Urology*. 52:333–339. doi:10.1080/21681805.2018.1545799.

Zhai, T.S., L.T. Hu, W.G. Ma, X. Chen, M. Luo, L. Jin, Z. Zhou, X. Liu, Y. Kang, Y.X. Kang, J.X. Zhang, H. Liu, J.Y. Lu, X.D. Yao, and L. Ye. 2021. Peri-prostatic adipose tissue measurements using MRI predict prostate cancer aggressiveness in men undergoing radical prostatectomy. *Journal of Endocrinological Investigation*. 44:287–296. doi:10.1007/s40618-020-01294-6.

Zhang, Q., L. Sun, J. Qi, Z. Yang, T. Huang, and R. Huo. 2014. Periprostatic adiposity measured on magnetic resonance imaging correlates with prostate cancer aggressiveness. *Urol J*. 11:1793–1799.

Zhao, S., C.M. Kusminski, and P.E. Scherer. 2021. Adiponectin, Leptin and Cardiovascular Disorders. *Circulation Research*. 136–149. doi:10.1161/CIRCRESAHA.120.314458.

Zwick, R.K., C.F. Guerrero-juarez, V. Horsley, V. Maksim, N. Haven, C. Biology, B. Gross, S. Cell, and N. Haven. 2019. Anatomical, physiological and functional diversity of adipose tissue. *Cell Metabolism*. 27:68–83. doi:10.1016/j.cmet.2017.12.002.Anatomical.

Figure legends

Figure 1: A new statistical approach to defining abundant PPAT relative to prostate volume

A) Left panel: Representative 3D projection and reconstruction of axial sections from T2-weighted mpMRI signals and regions of interest delineating the prostate (pink) and the PPAT (green); Right panel: single axial MRI sections from the base, middle, and apex of the prostate. The localization of PPAT, prostate (P) and the anatomical limits of PPAT are shown on single axial MRI section (B, Bladder; OM, Obturator Muscle; P, Prostate; PPAT, Periprostatic Adipose Tissue; PS, Pubic Symphysis; R, Rectum; SV, Seminal Vesicles; orange dotted lines indicate Denonvillier's fascia). Segmented area represents the region of interest delineating the prostate (pink) and the PPAT (green) for each single MRI section presented. **B)** Correlation between prostate weight recorded after prostatectomy and prostate volume measured on mpMRI (n=351). Linear regression was used to draw the slope of best fit and linear correlation coefficient (r^2) and P-value are indicated (p). **C)** Lack of correlation between prostate volume and the BMI of the patient (n=371); patients without PCa are indicated in red. **D)** Correlation between PPAT and prostate volume (n=371); patients without PCa are indicated in red. Linear regression was used to draw the slope of best fit and linear correlation coefficient (r^2) and P-value are indicated (p). **E)** Scatter plot of patients ranked according to PPAT abundance showing patients with low, mid and high PPAT abundance. PPAT abundance was calculated from the residual value for each patient with respect to the linear regression model in part D (n=371); patients without PCa are indicated in red. **F)** PPAT volume measured on MRI according to the abundance quartile (n=86-87 per quartile). **G)** Prostate volume of the patients in each abundance quartile (n=86-87 per quartile). **H)** BMI of the patients in each abundance quartile (n=86-87 per quartile). **I)** Distribution of patients' age in each abundance quartile (n=86-87 per quartile). Individual patient's data are indicated by dots, bars indicate means ± SEM. Statistical differences between groups were evaluated by ANOVA followed by a post-test for linear trend (*** $p< 0.001$).

Figure 2: Abundant PPAT is associated with aggressive PCa

A) Percentage of patients in the low, mid and high PPAT groups who have ISUP scores < 3 and ≥ 3. **B)** Raincloud plot of the percentage of undifferentiated cancer cells observed in prostate tumor slices from patients in the low, mid and high PPAT groups (Low, n= 88; Mid, n=176; High, n=87). **C)** Percentage of patients in the low, mid and high PPAT groups whose ISUP score was upgraded or not upgraded upon analysis of the tumors after prostatectomy. **D)** Multivariate analysis using logistic regression modelling of the effect of the indicated variables on the relative risk (odds ratio) that the PCa has an ISUP score ≥ 3 (Abundance, low, mid and high PPAT groups; Prostate, prostate volume (cm^3); Age (years); PSA, plasma PSA concentration (ng/ml); Gleason_bio, Gleason score on biopsy). **E-G)** Representative images

of prostate tumor slices from a patient in the 1st quartile of PPAT abundance (Low PPAT) and a patient in the 4th quartile (High PPAT) (left) after Masson's trichrome staining (E), immuno-staining for CD31 (F) and immuno-staining for CD68 (G). Immuno-stained tumor sections were counterstained with hematoxylin. Scale bars, 100µm. Quantification of the staining (right). Significant differences between groups were evaluated by Chi-square test for qualitative variables (A and C), by using ANOVA with post-test for linear trend (**p< 0.01; B) or Student's t test for quantitative variables (*p<0.05; ** p<0.01; E, F and G). Odds ratio were determined by using the multivariate logistic regression model (D).

Figure 3: PPAT expands by adipocyte hypertrophy with no associated inflammation

A) Representative images of PPAT sections stained with hematoxylin and eosin (H&E) and used to quantify adipocyte diameter in PPAT from patients in the low and high groups. The corresponding quantification mask is shown. Scale bars, 250µm. **B)** The size distribution (left panel) and mean diameters (right panel) of adipocytes in PPAT from patients in the low (n=12) and high (n=14) groups. **C)** Percentage of progenitor cells (CD45-/CD34+/CD31-) in the stroma-vascular fraction (SVF) of PPAT from patients in the low (n=8), mid (n=16) and high (n=11) groups, as quantified by flow cytometry quartile). **D-F)** Quantification of the concentration of adiponectin **(**D) and leptin (E) in the conditioned medium of PPAT from patients in the low (n=9), mid (n=9) and high (n=11) groups, and the adiponectin to leptin ratio (F). **G)** Percentage of cells in the SVF of PPAT from patients in the low (n=8), mid (n=15) and high (n=11) groups that are CD45+ leukocytes. **H**) Percentage of cells as in (G) that are low FSC/low SSC/CD45+/CD3+ T cells in the low (n=8), mid (n=15) and high (n=11) groups. **(I)** Percentage of cells as in (G) that are CD45+/CD14+ macrophages (all macrophages), CD45+/CD14+/CD206- recruited macrophages (CD206-), or CD45+/CD14+/CD206+ resident macrophages (CD206+) in the low (n=8), mid (n=15) and high (n=11) groups. All percentages in G-I were quantified by flow cytometry. **J-M)** Quantification of the concentrations of TNFα **(J)**, IL6 **(K)**, MCP1 **(L)** and IL1β **(M)** in the conditioned medium of PPAT from patients in the low, mid and high groups (n=8-10). Bars indicate means +/- SEM. Two-way ANOVA followed by Bonferroni post-test was used to analyze adipocyte diameter. Other statistical differences were evaluated by ANOVA with post-test for linear trend (*p<0.05; ** p<0.01).

Figure 4: Under-representation of mechano-sensing proteins in adipocytes from abundant PPAT

A) Principal component analysis of the proteomics datasets from adipocytes isolated from the PPAT of individual patients (each indicated by a dot and a label) in the low and high groups (n= 6-7 per group). The ellipses indicate grouping according to PPAT abundance. **B)** Volcano plot representing the log2 fold-change of the relative protein representation in the proteomics dataset and the -log10 of the p-value calculated by using limma differential expression analysis (n=6-7 per group), showing under-

represented (pink) and over-represented (green) proteins. **C**) Hierarchical clustering of differentially under-represented (pink) and over-represented (green) proteins in the PPAT of patients in the low (grey) and high (black) quartiles. **D)** Cellular components and biological functions of the over-represented (black) and under-represented (grey) proteins in the PPAT of patients in the high quartile, as determined by gene ontology enrichment terms. The -log10 of the q-Value are represented in x axis and the percentage of proteins that were differentially expressed in the pathways are mentioned in red on the side of each bar plot. **E)** Quantification of the indicated proteins in the PPAT of patients in the low and high quartile (n=6-7 per group) by mass spectrometry. **F)** Whole PPAT from patients in the low and high groups were stained with anti-YAP1 antibody and phalloidin (to stain actin and facilitate cell visualization) and DAPI (to stain DNA)**.** Representative maximum intensity projection of images obtained by 3D confocal microscopy are shown. Scale bars, 50 µm**. G)** Quantification of the indicated isoforms of tubulin, as in E (n=6-7 per group). **H)** Whole PPAT from patients in the low and high groups were stained with anti-ß-tubulin antibody and DAPI, as in F. **I)** Quantification of the indicated proteins, as in E (n=6-7 per group). Bars indicate means ± SEM. Statistical differences were calculated by using Student's T test. *$p < 0.05$; ** $p< 0.01$; *** $p<0.001$.

Figure 5: The collagen network in abundant PPAT is relatively loose

A) Whole PPAT from representative patients in the low and high groups were stained with picrosirius red to show collagen fibers, imaged in 3D by confocal microscopy (top), reconstructed in 3D (middle), and the reconstructed collagen fiber images were isolated and color-coded according to their diameter (bottom). Scale bars, 50 µm. **B-D)** Various morphometric parameters were quantified in 3D images of PPAT from patients in the low and high groups after collagen fiber reconstruction (n=9-16): total collagen volume (B), length of collagen fibers (C), and number of branches per collagen fiber (D). **E)** Quantification of hydroxyproline concentration in PPAT from patients in the low (n=18) and high groups (n=11). Bars indicate means ± SEM. Statistical differences were calculated by using Student's T test. *$p < 0.05$; ** $p< 0.01$.

Figure 6: Abundant PPAT exhibits increased collagen degradation likely by MMP9

A) Relative expression of genes encoding the indicated collagen isoforms in whole PPAT from patients in the low (n=13) and high qroups (n=11). **B)** Representative confocal images of PPAT stained with fluorescent collagen-hybridizing peptide (F-CHP). The maximum intensity projection of Z-stacked images (left panel) at low magnification and at higher magnification image (Zoom). The areas corresponding to the Zoom images are indicated by the orange dotted lines. Scale bars, 50 µm. F-CHP staining in 3D images was quantified (right panel; n=6-7). **C)** Relative expression of genes encoding the

indicated metalloproteinase (MMP) isoforms in PPAT from patients in the low (n=11) and high (n=10) quartiles. **D)** Relative MMP9 protein expression quantified in isolated mature adipocytes by mass spectrometry (n=6-7 per quartile). **E)** MMP9 enzyme activity in protein extracts of PPAT from patients in the low (n=13) and high quartiles (n=12). Bars indicate means ± SEM. Statistical differences were calculated by using Student's T test. *$p < 0.05$; *** $p< 0.001$.

Figure 7: COL6 remodeling is associated with high endotrophin production in abundant PPAT

A) Representative confocal images of PPAT from three patients in the low quartile (#1-3) and high quartile (#4-6) stained with an anti-collagen VI antibody that recognizes all collagen VI forms (pan collagen VI). Maximum intensity projections of Z-stacked images at low magnification are shown (left panels) and at higher magnification (Zoom). The areas corresponding to the Zoom images are indicated by the orange dotted lines. Scale bars, 50µm. **B)** Representative confocal immunofluorescence microscopy images of PPAT stained with anti-Pan collagen VI (pink) and anti-endotrophin (green) antibodies. 3D views of Z-stacked images (left). Scale bars, 50µm. Endotrophin staining was quantified on 3D images (right panel; n=8-9). **C)** ETP concentration in plasma from patients with PCa, as quantified by ELISA (Low, n= 20; Mid, n=42; High, n=20). **(D)** ETP concentration in urine from patients with PCa collected after prostate massage, as quantified by ELISA (Low, n= 17; Mid, n=32; High, n=13). Bars indicate means ± SEM. Statistical differences were calculated by using Student's T test (*$p < 0.05$ for B) and ANOVA with post-test for linear trend (**$p<0.01$ for C and D).

Figure 8: Collagen remodeling leads to inflammation-free expansion of periprostatic adipose tissue and promotes prostate cancer progression

As shown before (Roumiguié et al., 2022), PPAT exhibit a peculiar vascularization leading to chronic hypoxia and fibrosis that limits its expansion in obese individuals. To expand, collagen degradation occurs in high PPAT that exhibit hypertrophic adipocytes due to the increased expression of lipid transporters and the decreased expression of proteins involved in lipolysis, favoring lipid uptake over degradation. The decrease in ECM stiffness release the mechanical stress on adipocytes and allows the healthy expansion of high PPAT. The degradation of ECM and particularly COL VI, likely by MMP-9, contributes to the release of a matrikine, endotrophin. Endotrophin increases the aggressiveness of the adjacent PCa tumors by promoting cancer cell dedifferentiation and changes in the tumor microenvironment (increase in fibrosis, angiogenesis and macrophage infiltration). High levels of endotrophin are found in the urine of patients with abundant PPAT.

Legend of Supplementary Figures

Fig. S1: Subcutaneous and perirectal AT areas are correlated with BMI

Linear regression between the subcutaneous (**A,** n= 195**)** and perirectal (**B,** n=256**)** adipose tissue area measured on pre-operative mpMRI and the BMI of the patients. Linear regression was used to draw the slope of best fit and linear correlation coefficient (r^2) and P-value are indicated (p).

Fig. S2: NPFV is not an appropriate measure of PPAT abundance

A) Scatter plot of PCa patients ranked according to normalized periprostatic fat volume (NPFV) compared to PPAT abundance calculated by our model in Figure 1D (left panel), and the percentage of patients that were classified in different abundance quartiles depending on the method used to define abundance (right panel). Quartiles were defined according to NPFV ratio as low ratio (1st quartile) mid ratio (2nd and 3rd quartiles) or high ratio (4th quartile). **B-C)** Scatter plots of PPAT volume (B) and prostate volume (C) in individual patients in each quartile. Bars indicate means ± SEM. Differences between groups were determined by using ANOVA followed by Tuckey post-test. * $p< 0.05$; ** $p<0.01$; ***$p<0.001$. **D)** Multivariate analysis using logistic regression modelling of the effect of the indicated variables on the relative risk (odds ratio) that the PCa has an ISUP score ≥ 3 **(**Abundance, low, mid and high PPAT groups; Prostate, prostate volume (cm^3); Age (years); PSA, plasma PSA concentration (ng/ml); Gleason_bio, Gleason score on biopsy).

Fig. S3: Adipose progenitor cell and lymphocytes subsets are not modified according to PPAT abundance

A) Percentage of progenitor cell subsets (MSCA1+, MSCA1-/ CD271+ (CD271+) and MSCA1-/CD271- (-/-) in the stromal stromavascular fraction (SVF) of PPAT from patients in the low, mid and high groups, as quantified by flow cytometry. **B)** Percentage of lymphocytes subsets (CD4+: Cytotoxic T cell, CD8+: Helper T cell, CD4+/CD25+ Regulator T cell, CD19+: B lymphocytes) gated on the total lymphocytes (Low FSC/Low SSC/CD45+/CD3+) in the stromal vascular fraction (SVF) of PPAT from patients in the low, mid and high groups, as quantified by flow cytometry. Bars indicate means ± SEM. No statistical differences were observed by using Student's T test.

Fig. S4: Proteins involved in lipolysis and lipid uptake are under-represented and over-represented in abundant PPAT

A) Volcano plot representing the log2 fold-change of the relative protein representation in the proteomics dataset and the -log10 of the p-Value calculated by using limma differential expression analysis (n=6-7 /group), showing under-represented (red) and over-represented (green) proteins.

Proteins of interest are indicated by name of their genes. **B**) Scatter plot of the relative expression of *PNPLA2*, *LIPE* and *MGLL*, which encode lipolysis effectors determined by RT- qPCR, according to PPAT abundance determined by our model defined in Figure 1D (n=18). **C)** Scatter plots of the relative gene expression of *CD36*, *FABP4* and *SLC27A4*, which encode lipid transporters determined by RT-qPCR, according to PPAT abundance determined by our model defined in Fig. 1D (n=18).

Fig. S5: Absence of modifications of LOX or TIMP isoforms expression in low versus abundant PPAT. Relative expression of several genes encoding lysyl oxidase (LOX) or tissue inhibitor of metalloproteinase (TIMP) isoforms in PPAT from patients in the low and high quartiles (n=11 per quartile). Bars indicate means ± SEM. No statistical differences were observed by using Student's T test.

Table S1: Anthropometrical characteristics of the PCa patients

Characteristic	N = 351[1]
Age (years)	65 (60, 69)
BMI (kg/m^2)	25.48 (24.21, 27.76)
Missing	19
PPAT volume (cm^3)	43 (34, 53)
Subcutaneous AT area (cm^2)	35 (28, 44)
Missing	156
Prostate volume (cm^3)	44 (35, 60)
Perirectal AT area (cm^2)	25.9 (22.4, 30.3)
Missing	96

[1]Data are presented as the median value with inter-quartile range (IQR) in brackets. BMI, Body mass index

Table S2 : Clinical and pathological characteristics of the PCa patients

Characteristic	**N = 351**[1]
PSA (ng/ml)	7.0 (5.5, 10.0)
Missing	4
Tumor Volume (cm^3)	5.8 (3.2, 9.8)
Undifferentiated cancer cells (%)	40 (20, 65)
Missing	2
ISUP	
1	14 (4.0%)
2	193 (55%)
3	123 (35%)
4	20 (5.7%)
5	1 (0.3%)
pT	
2a	10 (2.8%)
2b	22 (6.3%)
2c	148 (42%)
3a	127 (36%)
3b	44 (13%)
Extra-prostatic extension	156 (44%)
Adjuvant treatment	
No	298 (85%)
Chemotherapy	27 (7.7%)
Hormonotherapy	2 (0.6%)
Radiotherapy	24 (6.8%)
Biochemical recurrence	38 (11%)
Missing	2

[1]Data are presented as the median value with inter-quartile range (IQR) in brackets or as percentage (%) in brackets
PSA, prostate specific antigen

Table S3 : Clinical and pathological characteristics of the PCa patients according to PPAT abundance

Characteristic[1]	Low, N = 88	Mid, N = 176	High, N = 87	p-value
PSA (ng/ml), Median (IQR)	7.0 (5.1, 9.6)	7.0 (5.2, 9.0)	8.0 (6.1, 11.1)	0.0179[2]
(Missing)	1	3	0	
Tumor Volume (cm^3), Median (IQR)	5.1 (2.8, 9.5)	6.2 (3.3, 9.9)	6.0 (3.0, 9.9)	0.4400[2]
Gleason score on biopsies ≥ 3, n (%)	21 (24)	55 (31)	30 (34)	0.2790[3]
Missing	0	1	0	
Undifferentiated cancer cells (%), Median (IQR)	28 (10, 60)	40 (20, 70)	55 (22, 72)	0.0008[2]
(Missing)	0	2	0	
ISUP ≥ 3, n (%)	26 (30)	73 (41)	45 (52)	0.0115[3]
Upgrading, n (%)	10 (15)	30 (25)	22 (39)	0.0104[3]
Missing	21	56	30	
pT n (%)				0.2413[3]
2a or 2b	6 (6.8)	17 (9.7)	9 (10)	
2c	42 (48)	67 (38)	39 (45)	
3a	35 (40)	66 (38)	26 (30)	
3b	5 (5.7)	26 (15)	13 (15)	
Extra-prostatic extension	39 (44)	81 (46)	36 (41)	0.7752[3]

[1]Data are presented either as the median value with inter-quartile range (IQR) in brackets or percentage (%) in brackets. PSA, prostate specific antigen

Kruskal-Wallis rank sum test

[3] Pearson's Chi-squared test

Table S4: Clinical and pathological characteristics of the PCa patients according to NPFV

Characteristic[1]	**Low**, N = 88	**Mid**, N = 87	**High**, N = 87	**p-value**
PSA (ng/ml), Median (IQR)	7.0 (5.8, 9.8)	7.2 (5.4, 9.8)	7.0 (5.5, 9.8)	0.6948[2]
Missing	0	4	0	
Tumor Volume (cm^3), Median (IQR)	6.8 (3.7, 10.6)	5.6 (3.2, 9.4)	5.8 (2.8, 9.0)	0.2857[2]
Gleason score on biopsy≥3, n (%)	24 (27)	53 (30)	29 (33)	0.6835[3]
Missing	0	1	0	
Undifferentiated cancer cells (%), Median (IQR)	38 (19, 60)	35 (16, 70)	40 (20, 68)	0.5589[2]
Missing	0	2	0	
ISUP ≥ 3, n (%)	32 (36)	73 (41)	39 (45)	0.515[3]
Upgrading, n (%)	14 (22)	34 (28)	14 (24)	0.6503[3]
Missing	24	54	29	
pT, n (%)				0.6643[3]
2a or 2b	8 (9.1)	16 (9.1)	8 (9.2)	
2c	39 (44)	74 (42)	35 (40)	
3a	33 (38)	66 (38)	28 (32)	
3b	8 (9.1)	20 (11)	16 (18)	
Extraprostatic extension, n (%)	36 (41)	80 (45)	40 (46)	0.74053

[1]Data are presented as the median value with inter-quartile range (IQR) in brackets or as number of values and percentage (%) in brackets. PSA, prostate specific antigen
[2] Kruskal-Wallis rank sum test
[3] Pearson's Chi-squared test

Table S5: Anthropometrical characteristics of the patients in the cohort used for endotrophin quantification in biological fluids

Characteristic	N = 78[1]
Age (years)	66.0 (61.8, 69.0)
Missing	6
BMI (kg/m^2)	25.68 (24.32, 27.15)
Missing	12
PPAT Volume (cm^3)	41 (33, 52)
Prostate Volume (cm^2)	48 (38, 62)
PPAT Abundance (Group)	
Low	20 (26%)
Mid	37 (47%)
High	21 (27%)
[1]	

[1]Data are presented as the median value with inter-quartile range (IQR) in brackets. BMI, Body mass index

Table S6: Clinical and pathological characteristics of the patients in the cohort used for endotrophin quantification in biological fluid

Characteristic	N = 78[1]
PSA (ng/ml)	6.0 (4.0, 10.0)
Missing	1
Tumor Volume (cm^2)	3 (2, 6)
Missing	37
Undifferentiated cancer	30 (10, 65)
Missing	6
ISUP	
0	1 (1.3%)
1	25 (32%)
2	31 (40%)
3	13 (17%)
4	4 (5.2%)
5	3 (3.9%)
Missing	1
pT	
pT2a or 2b	4 (5.3%)
pT2c	48 (64%)
pT3a	16 (21%)
pT3c	7 (9.3%)
Missing	3

[1]Data are presented as the median value with inter-quartile range (IQR) in brackets or as percentage (%) in brackets
PSA, prostate specific antigen

Table S7: List of primers used for RT-qPCR

Gene name	Reference
18S	Hs99999901_s1
CD36	Hs00354519_m1
FABP4	Hs01086177_m1
LIPE	Hs00943410_m1
MGLL	Hs00996004_m1
PNPLA2	Hs00386101_m1
SLC27A4	Hs00192700_m1
COL1A1	Hs00164004_m1
COL3A1	Hs00943809_m1
COL6A1	Hs01095585_m1
COL6A2	Hs00365167_m1
COL6A3	Hs00915125_m1
MMP14	Hs00237119_m1
MMP11	Hs00968295_m1
MMP2	Hs01548727_m1
MMP9	Hs00957562_m1
BMP1	HS00241807_m1
LOX	Hs00942483_m1
LOXL1	Hs00935937_m1
TIMP1	Hs99999139_m1
TIMP2	Hs00234278_m1
TIMP3	Hs00165949_m1
TIMP4	Hs00162784_m1

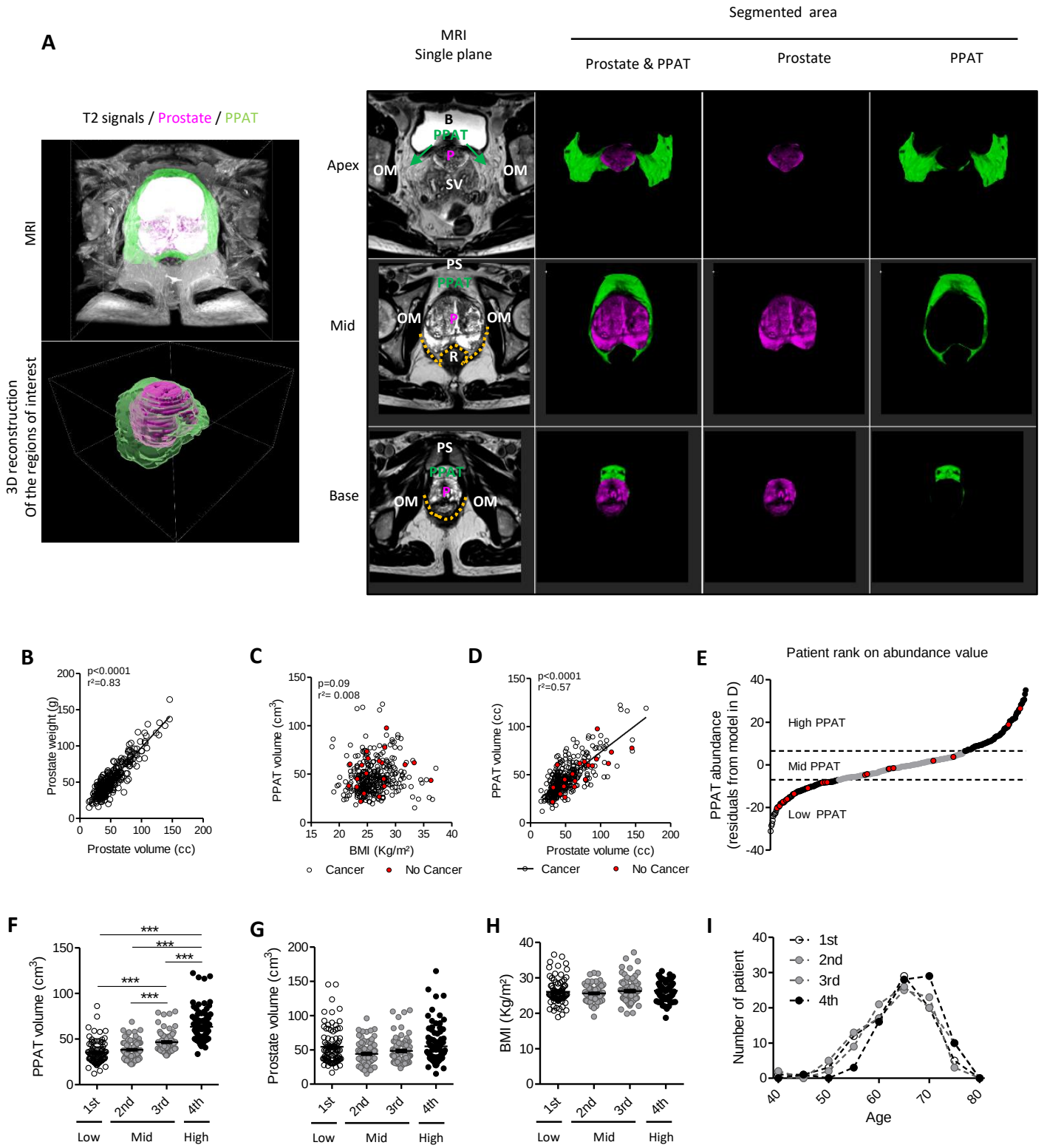

Figure 1. A new statistical approach to defining abundant PPAT relative to prostate volume

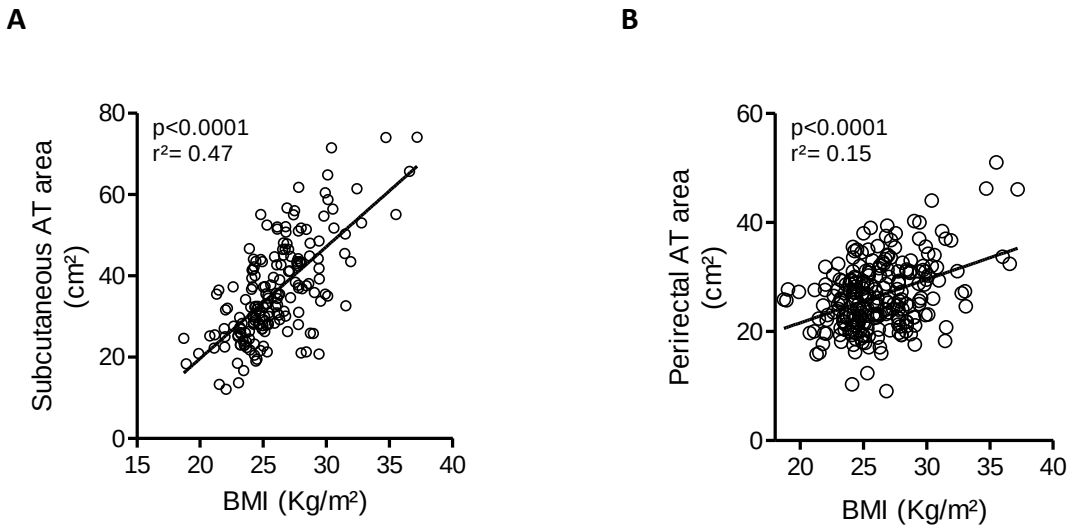

Figure S1. Subcutaneous and perirectal AT areas are correlated with BMI

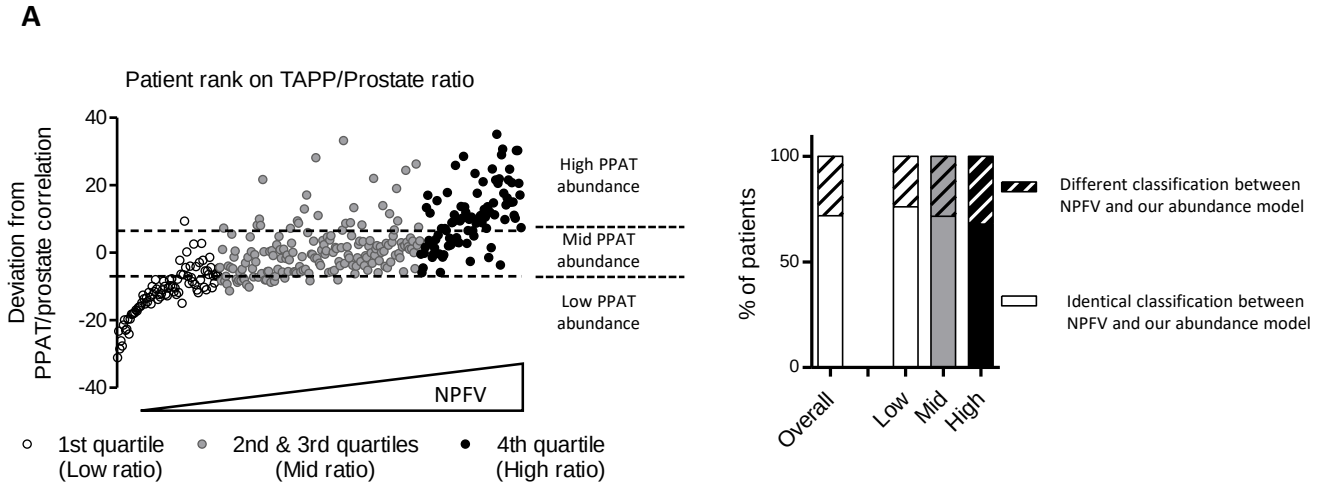

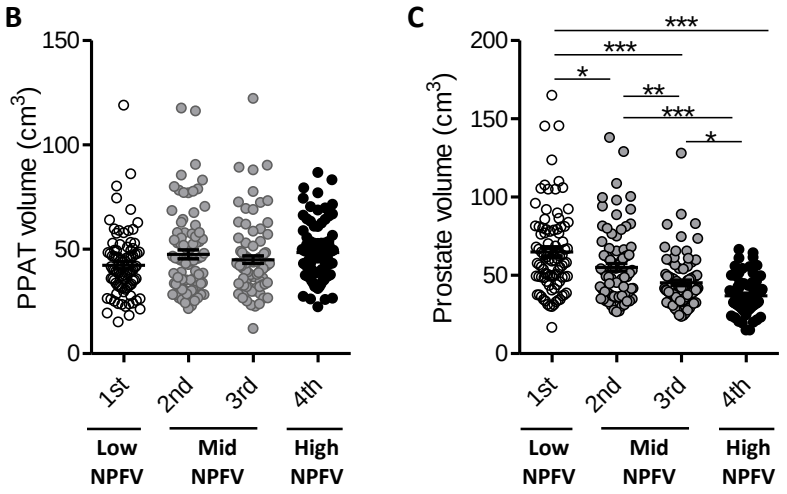

D

Predictor (ISUP ≥ 3)		N	Odds ratio	p
NPFV	Low	88	Reference	
	Mid	172	1.26 (0.67, 2.43)	0.477
	High	87	1.27 (0.58, 2.83)	0.550
Prostate		347	1.00 (0.98, 1.01)	0.599
Age		347	1.01 (0.97, 1.05)	0.762
PSA		347	1.08 (1.02, 1.14)	0.009
Gleason_bio	1	73	Reference	
	2	170	2.21 (1.10, 4.79)	0.033
	3	71	13.74 (6.10, 33.27)	<0.001
	4	33	23.66 (7.84, 84.55)	<0.001

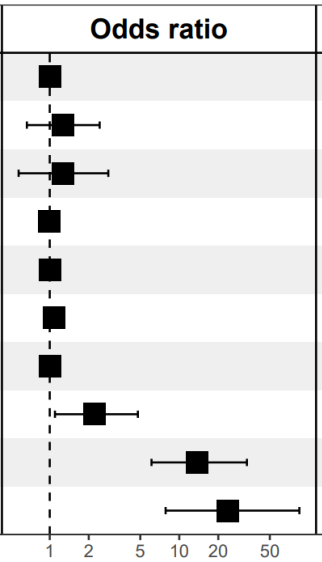

Fig. S2. NPFV is not an appropriate measure of PPAT abundance

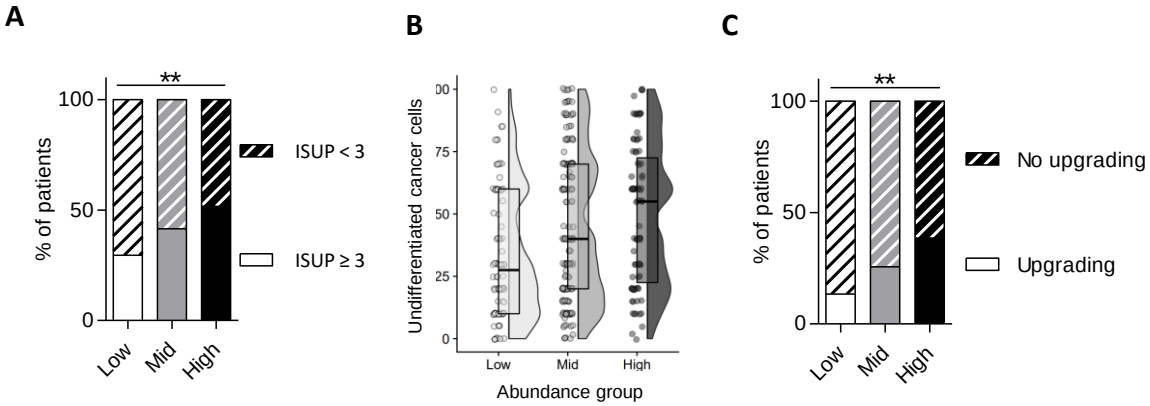

D

Predictor (ISUP ≥3)		N	Odds ratio	Odds ratio (CI)	p
Abundance	Low	87		Reference	
	Mid	173		1.71 (0.90, 3.32)	0.10
	High	87		2.43 (1.18, 5.11)	0.02
Prostate		347		1.00 (0.98, 1.01)	0.50
Age		347		1.00 (0.96, 1.04)	0.92
PSA		347		1.08 (1.02, 1.14)	0.01
Gleason_bio	1	73		Reference	
	2	170		2.36 (1.16, 5.15)	0.02
	3	71		14.33 (6.31, 35.01)	<0.001
	4	33		26.39 (8.62, 95.72)	<0.001

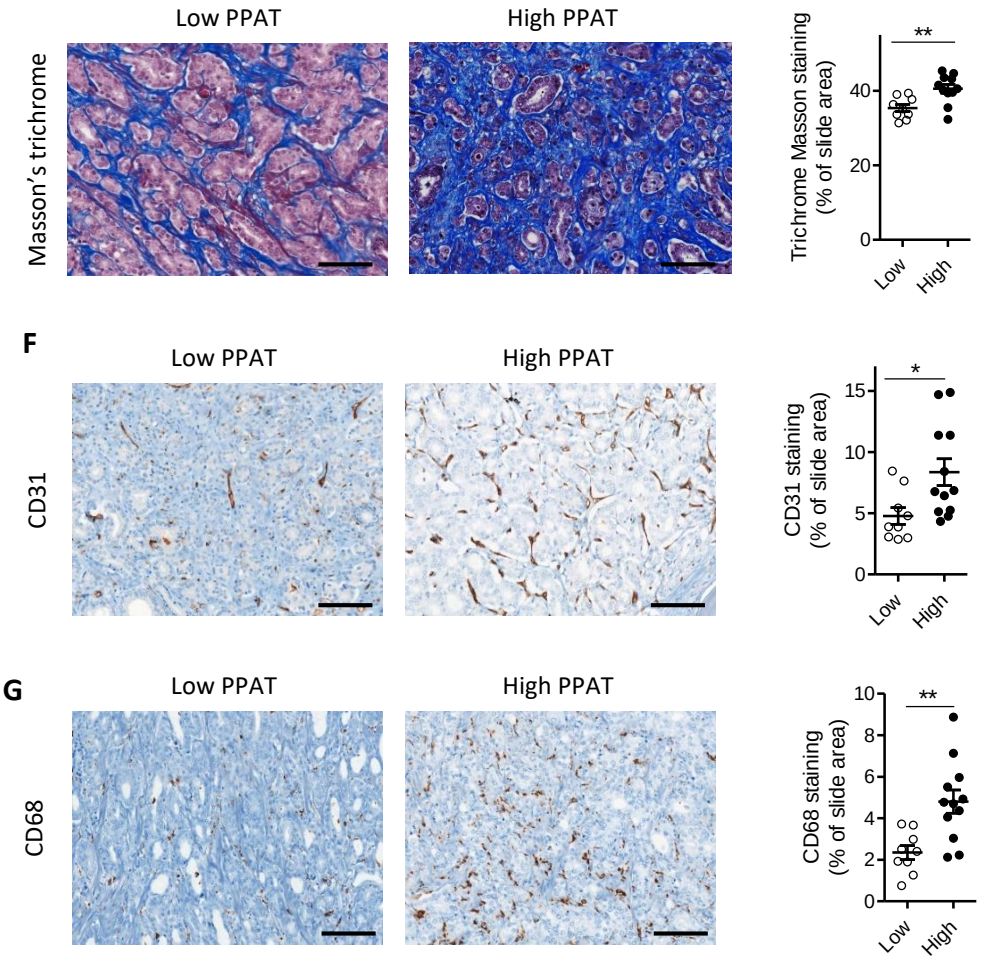

Figure 2. Abundant PPAT is associated with aggressive tumors

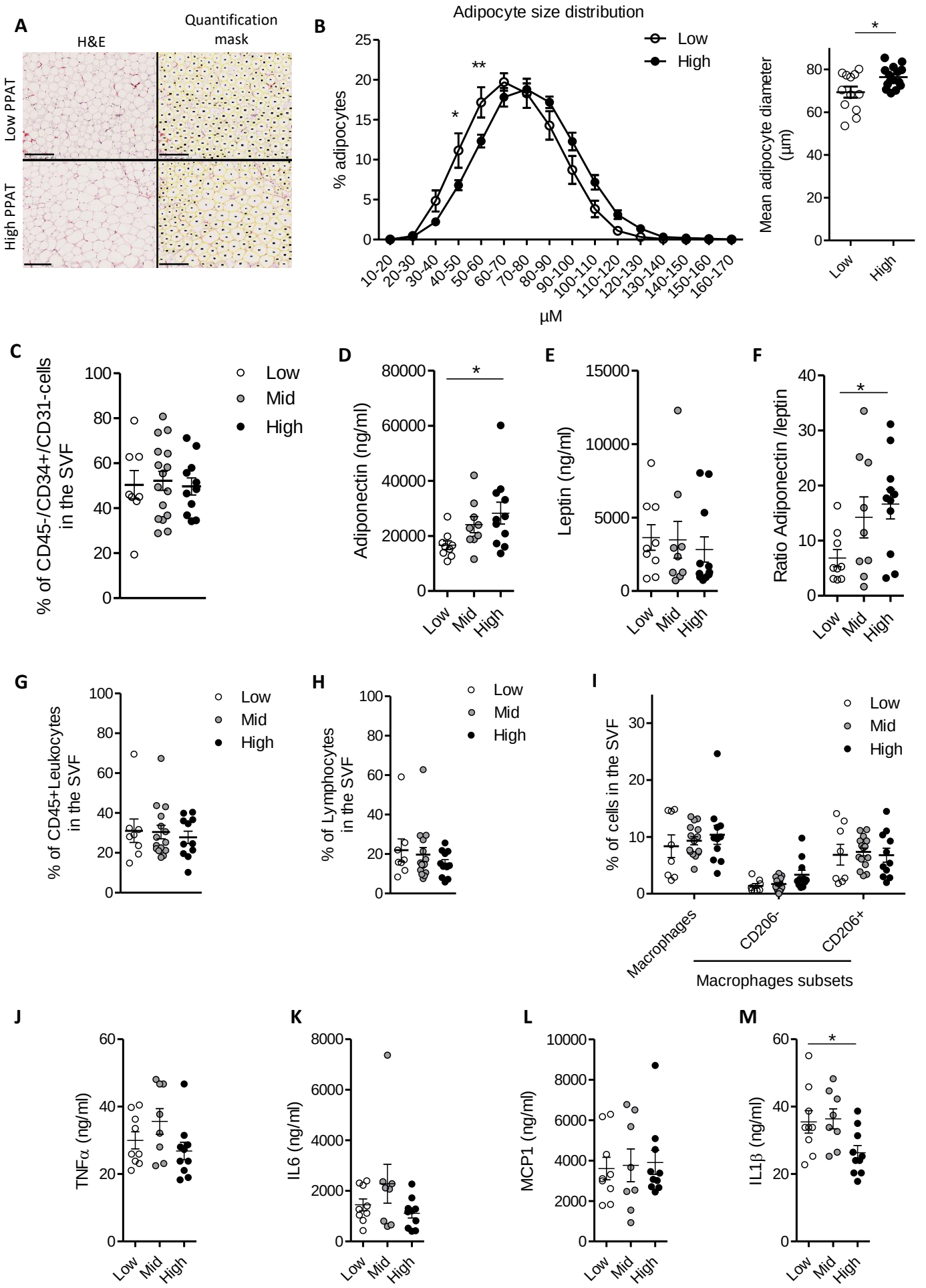

Figure 3: PPAT expands by adipocyte hypertrophy with no associated inflammation

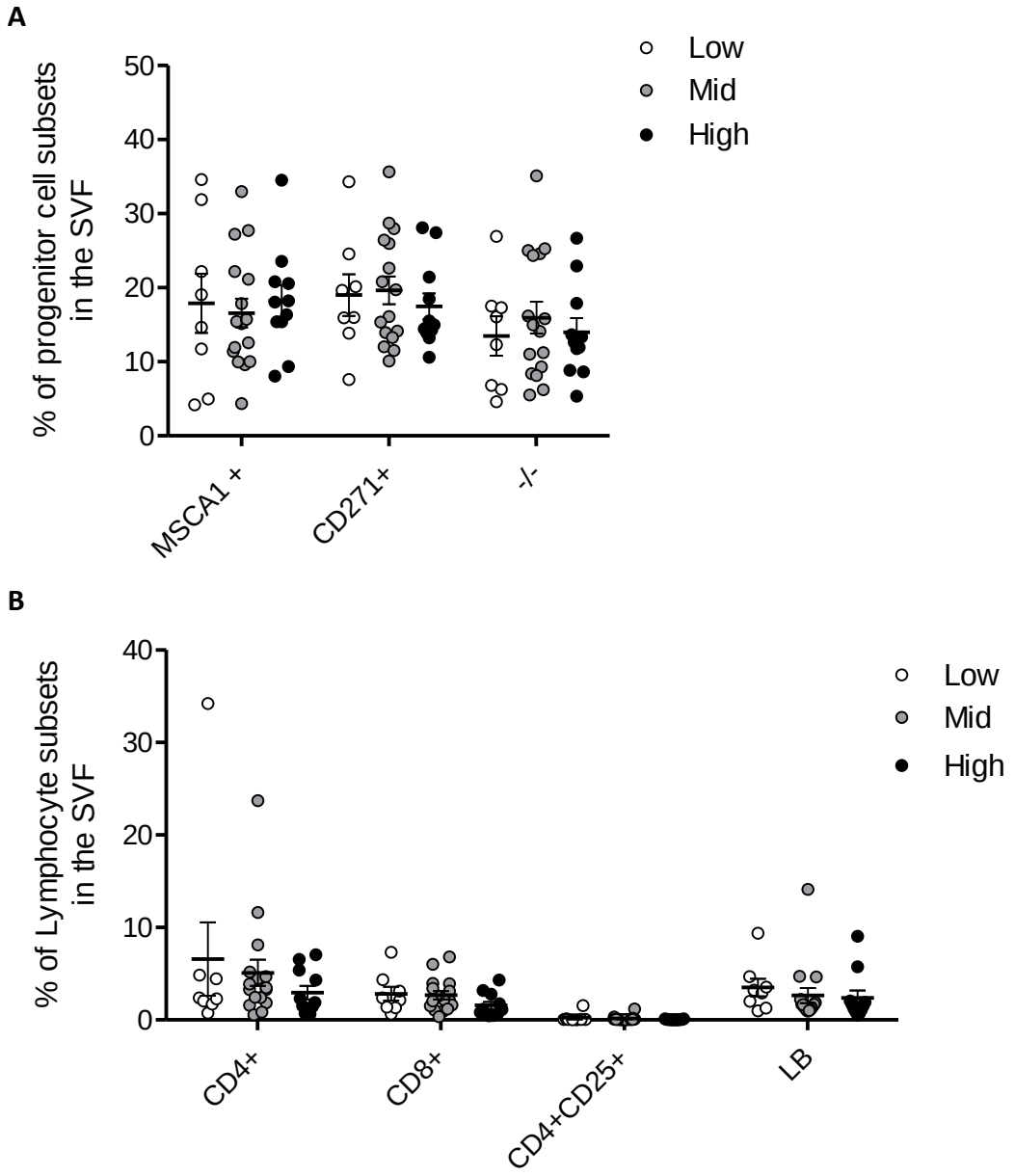

Figure S3. Adipose progenitor cell and lymphocytes subsets are not modified according to PPAT abundance

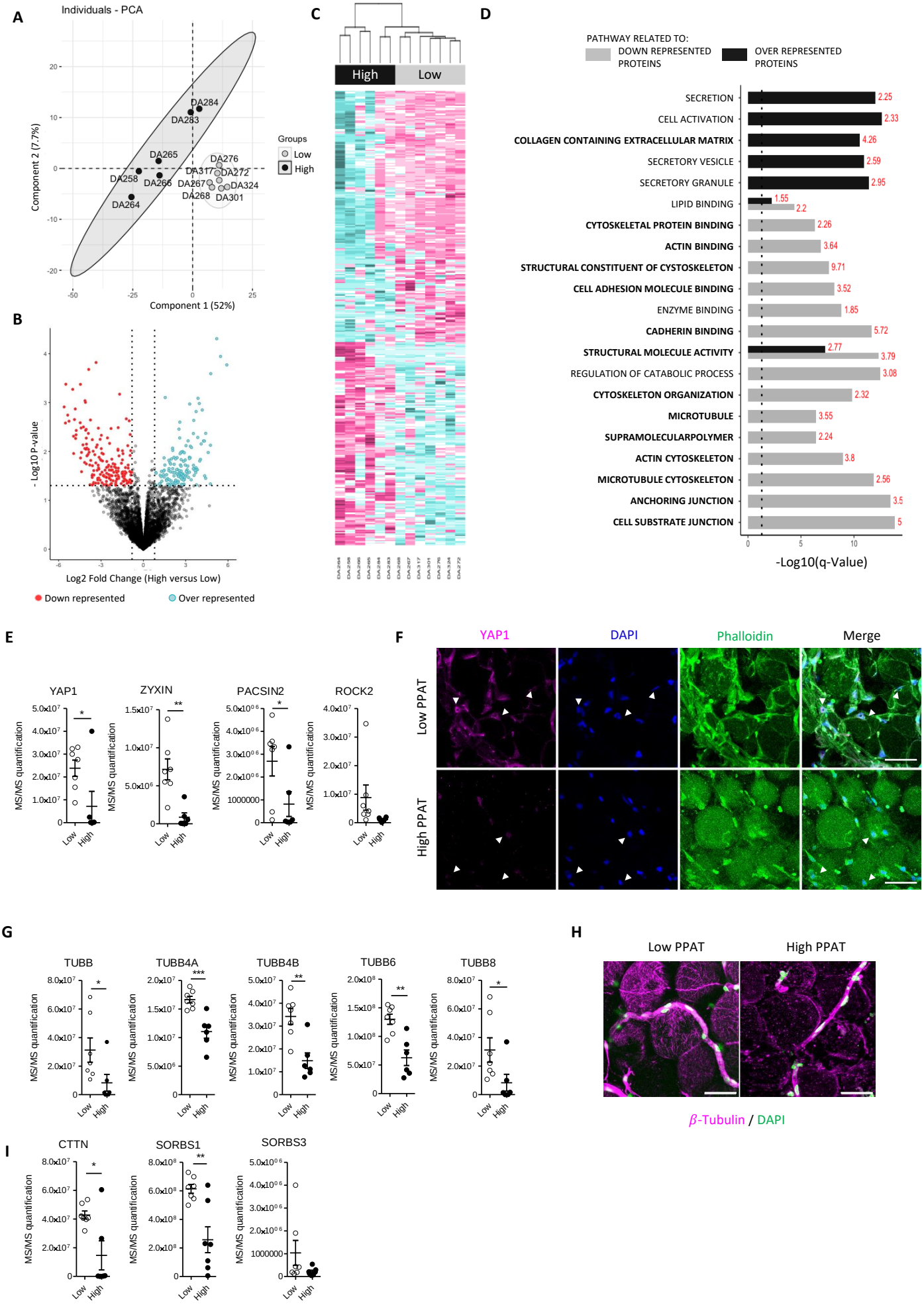

Figure 4: Under-representation of mechano-sensing proteins in abundant PPAT

A

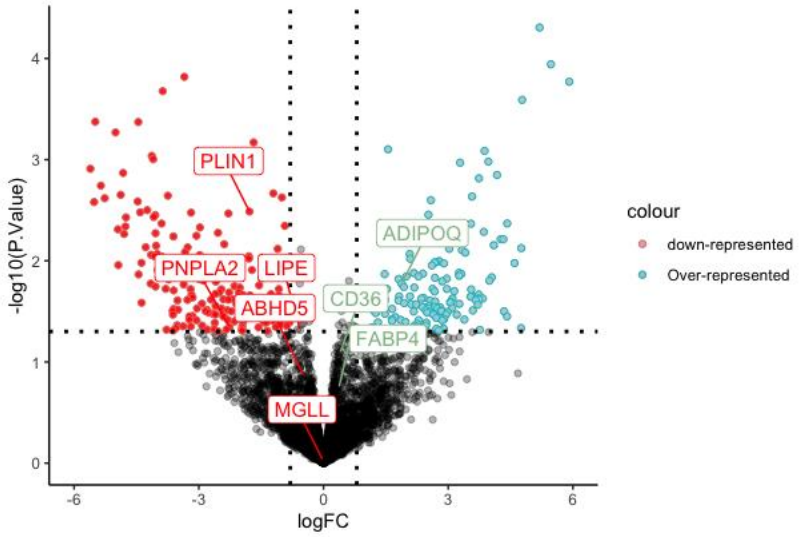

B

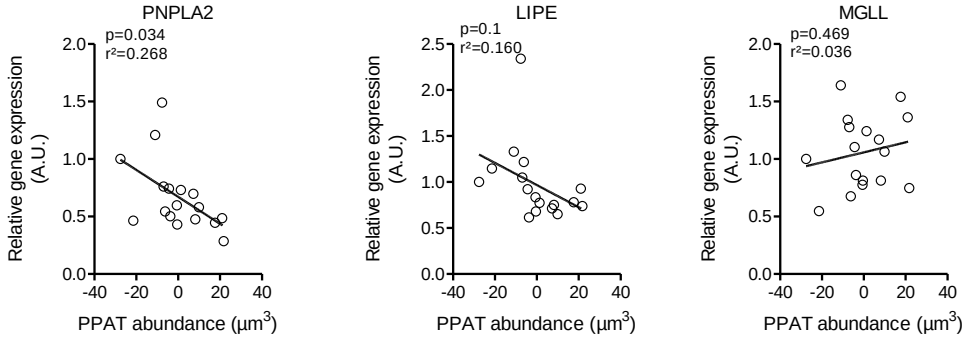

C

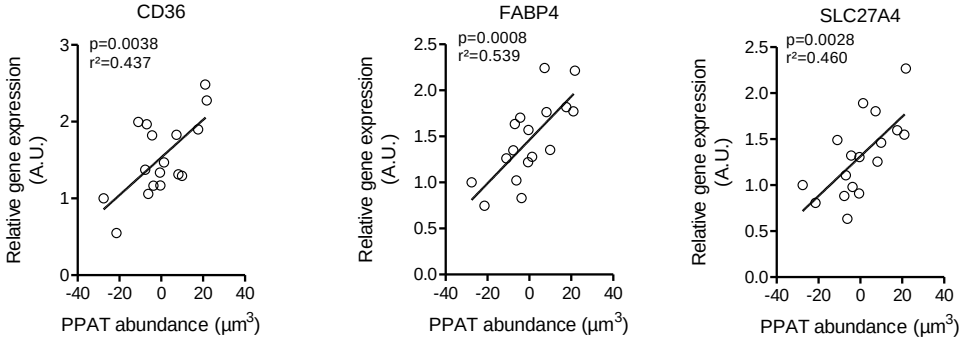

Figure S4. Proteins involved in lipolysis and lipid uptake are under-represented and over-represented in abundant PPAT

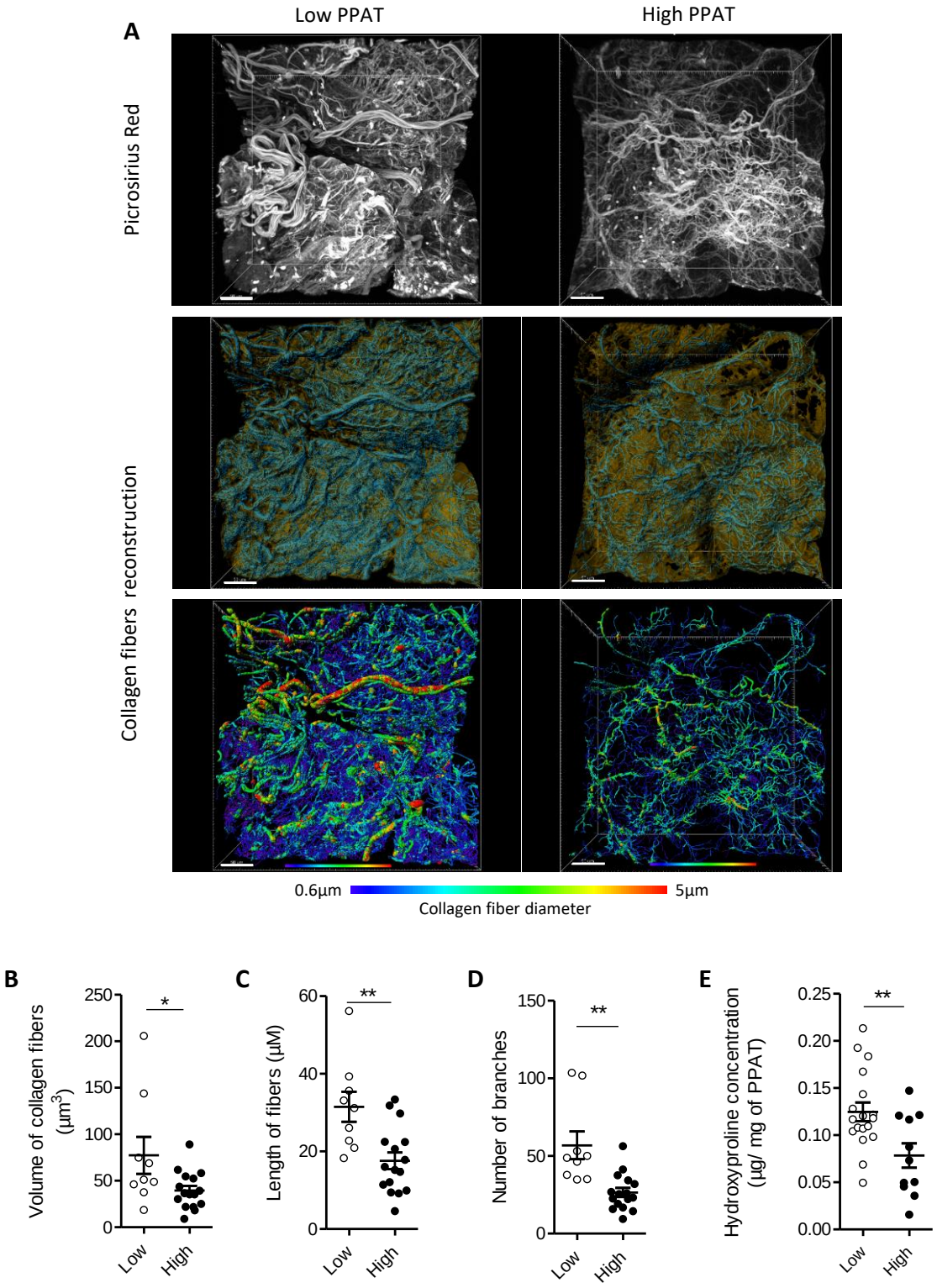

Figure 5: The collagen network in abundant PPAT is relatively loose

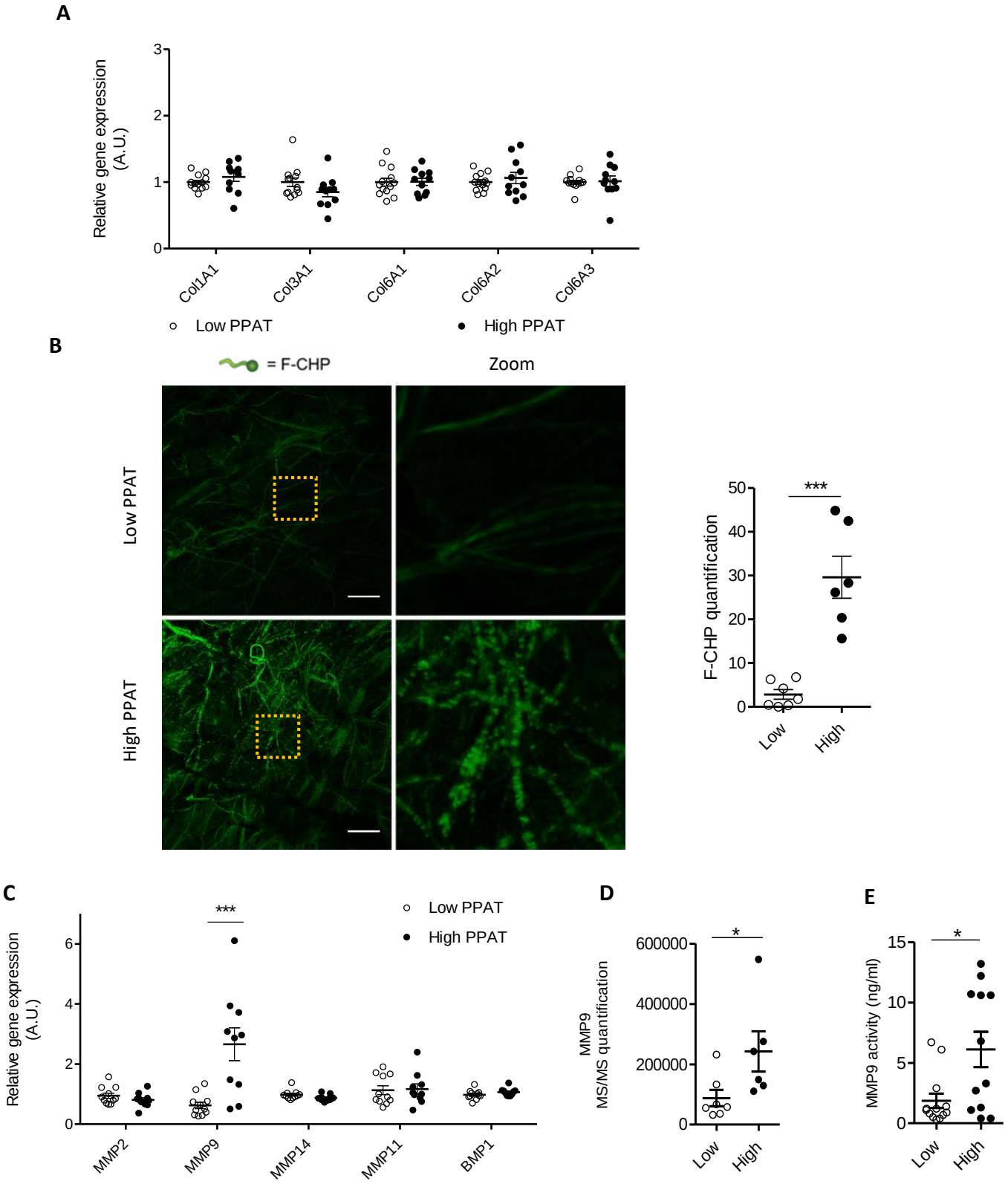

Figure 6: Abundant PPAT exhibits increased collagen degradation likely by MMP9

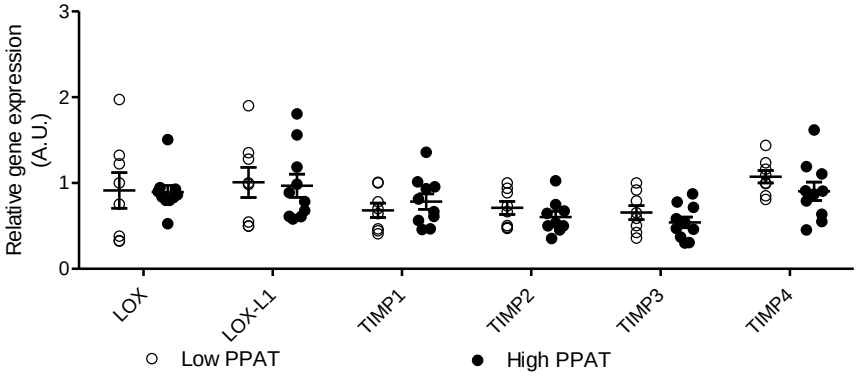

Figure S5. Absence of modifications of LOX or TIMP isoforms expression in low versus abundant PPAT.

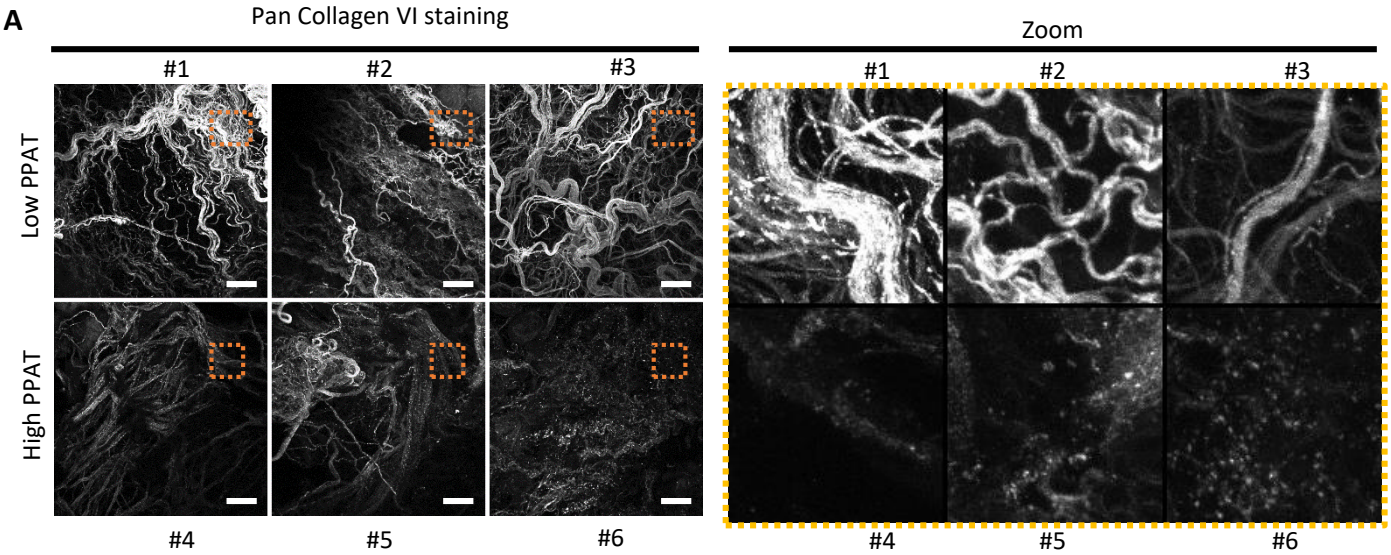

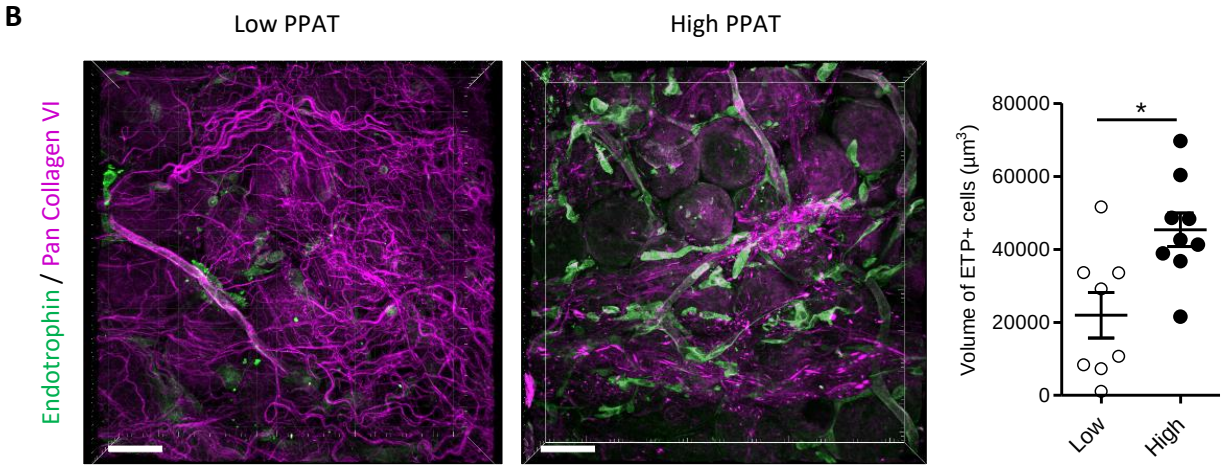

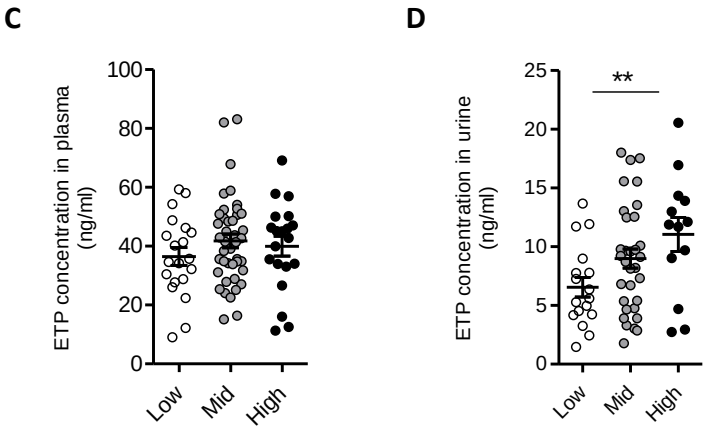

Figure 7: COL6 remodeling is associated with high endotrophin production in abundant PPAT

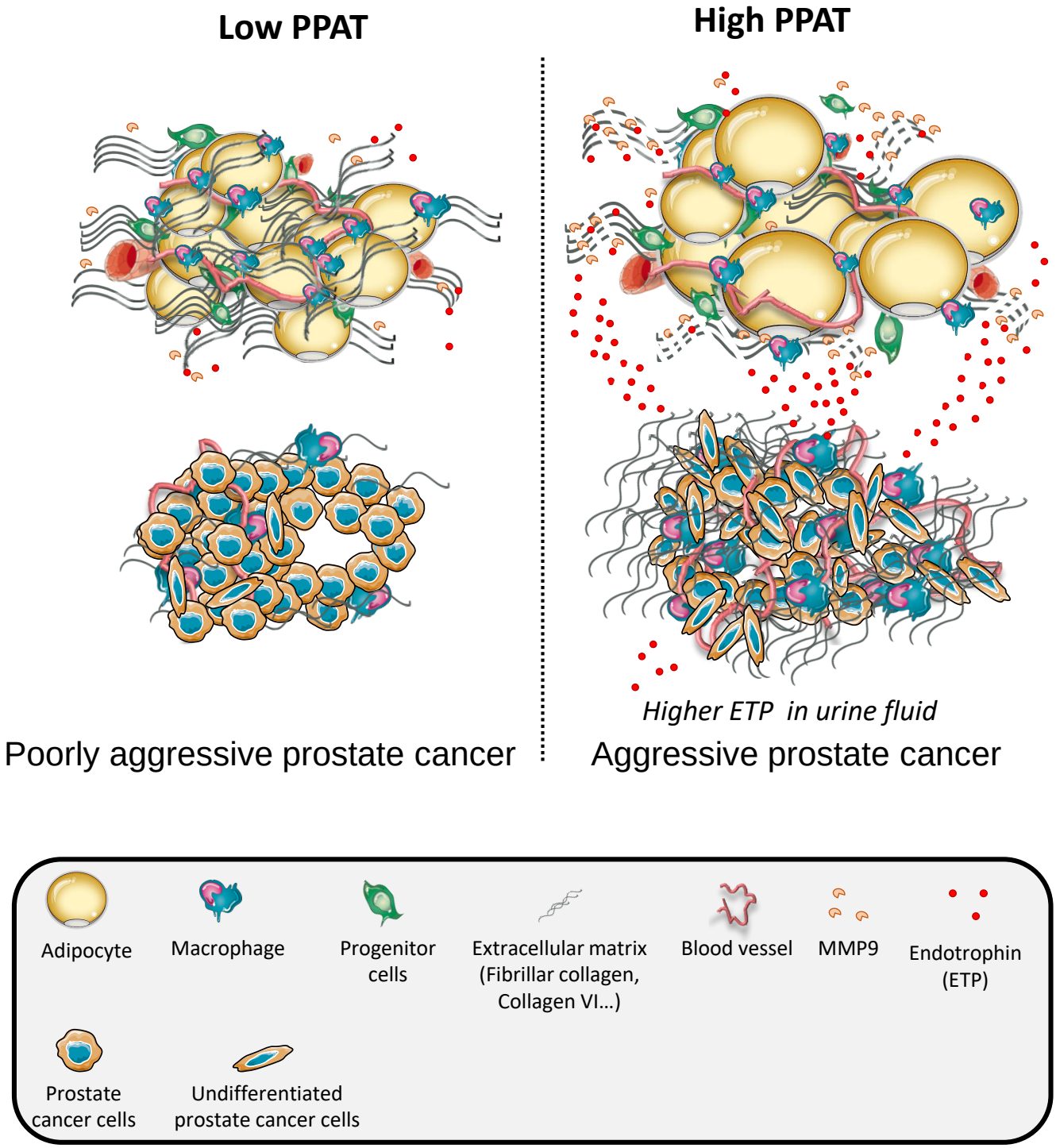

Figure 8: Collagen remodeling leads to inflammation-free expansion of periprostatic adipose tissue and promotes prostate cancer progression